UNIVERSITÀ DEGLI STUDI DI PADOVA

Dipartimento di Fisica e Astronomia

Corso di laurea magistrale in

Astronomia

Accreting neutron stars with multi-polar magnetic field

in Ultraluminous X-ray Sources

Relatore: prof. Roberto Turolla

Co-relatore: dott. Luca Zampieri

Laureando: Achille Fiore

Matricola 1040353

Anno Accademico

2016/2017

Contents

Abstract

Le sorgenti X ultraluminose (Ultraluminous X-ray Sources, ULXs) sono interpretate come oggetti compatti in accrescimento in galassie esterne. La loro luminosità supera il limite di Eddington per un buco nero di $10\,M_\odot$. La recente scoperta di tre ULXs pulsanti fa ritenere che in questo caso l'oggetto compatto sia una stella di neutroni con un elevato campo magnetico B ($B > 12\,G$). Quest'ultimo diminuisce l'opacità di electron scattering rispetto all'opacità di Thomson, consentendo così luminosità di accrescimento più elevate. Il calcolo della luminosità di accrescimento per una stella di neutroni magnetizzata è stato fatto in questa Tesi seguendo l'implementazione ed il relativo procedimento iterativo proposto da Mushtukov et al. (2015b).

Tuttavia la ULX pulsante NGC 5907 ULX-1 non può essere spiegata da questo modello (Israel et al. 2017b). Ipotizzando che il campo magnetico della stella di neutroni abbia una topologia più complessa del caso dipolare, è possibile riprodurre il modello di Mushtukov et al. (2015b) assumendo che il campo magnetico della stella di neutroni abbia un termine di ordine maggiore nel suo sviluppo multipolare (come suggerito da Israel et al. 2017b). I risultati di quest'ultimo modello, da noi implementato, sono in grado di rendere conto delle proprietà osservative di NGC 5907 ULX-1, confermando l'ipotesi di Israel et al. (2017b).

Chapter 1

Ultraluminous X-ray Sources

It is widely accepted that the majority of Ultraluminous X-ray Sources (ULXs) are accreting compact object hosted in external galaxies; their luminosity exceeds the Eddington limit for a $10\,M_\odot$ black hole and challenges the standard accretion model. In this Chapter we shortly review their properties: Sec. 1.1-1.3 introduce the theoretical framework and the scenarios proposed to account for their luminosity; in Sec. 1.4 some of their observational properties are discussed in more detail, referring in particular to the case of ULXs with black holes.

1.1 Introduction

Ultraluminous X-ray Sources (ULXs) are X-ray non-nuclear, point-like sources in external galaxies whose luminosity $\mathcal{L}$ exceeds the Eddington limit for a $10\,M_\odot$ compact object, i. e. $\mathcal{L} \gtrsim 10^{39}\,\mathrm{erg\,s^{-1}}$. They were first detected with the *Einstein* satellite but they could not be studied in detail because of its poor spatial

resolution (see e. g. Fabbiano & Trinchieri 1987).

If the accreting compact object is a Black Hole (BH), accounting for an observed luminosity higher than $10^{39}\,\mathrm{erg\,s^{-1}}$ might seem feasible if the BH is more massive than $10\,\mathrm{M}_{\odot}$. But the current models of stellar evolution show that BHs of stellar origin with mass greater than $\sim 100\mathrm{M}_{\odot}$ cannot form (Zampieri & Roberts 2009, Mapelli et al. 2009, Belczynski et al. 2010). An alternative possibility is that the accreting compact object is an intermediate mass BH, with a mass in excess of $100\,\mathrm{M}_{\odot}$ (e. g. Colbert & Mushotzky 1999). However, significant evidence of the occurence of intermediate mass BH in ULXs is limited to a few sources (most notably HLX-1 ESO 243-49, Farrell et al. 2009).

On the other hand, in certain conditions the luminosity could be greater than $\sim 10^{39}\,\mathrm{erg\,s^{-1}}$ because the source is emitting above the Eddington limit or it is beamed. In the latter case, the radiative flux S_O can be expressed as:

$$S_O = \frac{\mathcal{L}}{\Omega R^2}\,, \tag{1.1.1}$$

where Ω is the solid angle within which the flux S_O is emitted. If $\Omega < 4\pi$, the actual luminosity emitted by the source is:

$$\mathcal{L} = \frac{\Omega}{4\pi}\mathcal{L}'\,, \tag{1.1.2}$$

where $\mathcal{L}'$ is the apparent isotropic luminosity. Hence the observed super-Eddington luminosities of ULXs might be explained in part by the fact that the emission is beamed (i. e. geometrically confined within a solid angle $\Omega < 4\pi$). Thus, a BH-powered ULX can be modelled by a midly-beamed emission from a $10 \div 100\,M_{\odot}$ BH.

We will discuss this scenario and the possibility that emission overcomes the Eddington limit in more detail in the following Sections.

1.2 The Eddington limit

Accretion onto compact objects is a physical process invoked for explaining many phenomena in high-energy astrophysics, especially those emitting in the X-ray and gamma-ray bands. The standard accretion theory tells us that in spherical symmetry and in stationary condition the maximum luminosity emitted by an accreting compact star is the well-known **Eddington limit** $\mathcal{L}_{\rm Edd}$.

Indeed assuming a spherically symmetric accretion of matter onto the surface of an object of mass M and radius R and considering a pure-hydrogen gas, infalling electrons emit radiation (e.g. through free-free process) that will afterwards interact with the other electrons via Thomson scattering. Electrons and protons dragged (by Coulomb forces) with them are simultaneously:

- *attracted inwards* by the gravitational field;
- *accelerated outwards* by the radiative force.

Indicating with $k_{\rm T}$ the Thomson opacity and neglecting the electron mass m_e with respect to the proton mass m_p, the balance of the two opposite forces returns:

$$\frac{GM}{R^2} m_p - \frac{k_{\rm T}}{c} \frac{\mathcal{L}_{\rm Edd}}{4\pi R^2} = 0\,. \tag{1.2.1}$$

The corresponding limiting luminosity, known as the Eddington luminosity, is:

$$\mathcal{L}_{\rm Edd} = \frac{4\pi G M m_p c}{k_{\rm T}} = 1.3 \times 10^{38} \left(\frac{M}{\mathrm{M}_\odot}\right) \mathrm{erg\,s^{-1}}\,. \tag{1.2.2}$$

As already mentioned above, in writing equation (1.2.2) we have made four crucial assumptions:

- spherical symmetry;
- stationarity of the accretion-flow;
- pure hydrogen accreting gas;

- Thomson opacity.

Relaxing one or more of these hypotheses may provide a *super-Eddington luminosity*.

1.3 Effective gravitational potential and mass transfer

In this Section we briefly summarize the properties of the effective gravitational potential of a ULX in a binary systems. We start from the solution of the *Circular Restricted Three-body Problem*: a small point-mass m moves in the gravitational potential of two masses M_1 and M_2 orbiting around each other, with $m \ll M_1, M_2$.

Let the two objects be in the position $r_1 = (x_1, 0)$ and $r_2 = (x_2, 0)$ in a corotating frame of reference (O, x, y), as displayed in Fig. 1.1. In the position $r = (x, y)$ the point-mass particle feels the gravitational potential $\Phi(r)$ (see e. g. Frank et al. 2002):

$$\Phi(r) = -\frac{M_1}{d_1(r)} - \frac{M_2}{d_2(r)} - \Omega^2 r^2 \,, \tag{1.3.1}$$

where $d_1(x, y) = \sqrt{x^2 + y^2 - r_1^2}$ and $d_2(x, y) = \sqrt{x^2 + y^2 - r_1^2}$ are the distances between the istantaneous position of the point-mass object and the center of mass of M_1 and M_2 respectively. With these results in mind, let us then suppose that:

- M_1 is a compact star, e. g. a BH.
- M_2 is a *normal star*[1].

The extrema of $\Phi(r)$ are generally referred to as *Lagrangian points*. Gas moves along the equipotential lines and can reach M_1 via the inner Lagrangian point

[1] I. e. a non-degenerate star.

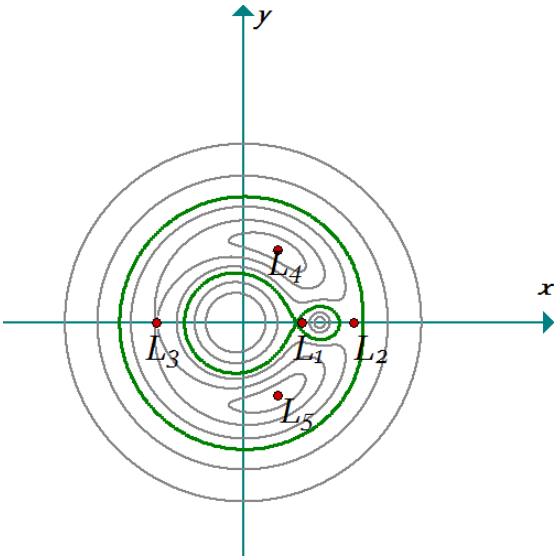

Figure 1.1: Contour lines of the potential $V(x, y)$; the green contour represents the Roche Lobe of the system.

L_1, hence forming an accretion disc. The limiting equipontential surface that surrounds both stars is usually called *Roche Lobe*. Plasma can reach L_1 basically in two ways:

- if the star does not fill entirely its own lobe, matter expelled through stellar wind can reach L_1;

- if the star instead fills its lobe, matter from the surface of the star can flow directly through L_1 acquiring a huge angular momentum and establishing the *Roche-lobe overflow* regime.

As we will see in Sec. 2.3.1 the latter case is the dominant mass transfer process in ULXs.

1.4 BH-powered ULXs

We started assuming that ULXs are accreting Black Hole Binaries (BHBs). In fact, the present work will focus mostly on the physics of ULX Pulsars (see Chapter 2), but in this Section the main properties of the BH-powered ULXs are briefly summarized.

1.4.1 Super Eddington accretion

Different scenarios for BH-powered ULXs may be put forward considering:

- beamed emission with $b = \Omega/4\pi < 1$ (see Sec. 1.1);
- different BH masses M in the range $10 \div 100\,\mathrm{M}_\odot$ (see Sec. 1.1);
- super-Eddigton accretion with $\dot{m} > 1$, where $\dot{m} = \dot{M}/\dot{M}_{\mathrm{Edd}}$.

The first two possibilities have been shortly addressed above. The latter is discussed in detail in Feng & Soria 2011. Here we simply note that exceeding the Eddigton limit may be possible if the mass-accretion rate $\dot{M}$ itself exceeds the Eddington mass-accretion rate $\dot{M}_{\mathrm{Edd}}$. In these conditions the disc becomes geometrically thick (Poutanen et al. 2007). As a consequence, the approximation of thin disc (Shakura & Sunyaev 1973) must be relaxed. The timescale for the plasma-inflow becomes smaller than that for the diffusion of photons, that are then carried inward towards the BH (Abramowicz et al. 1988). For this reason this accretion flow is referred to as Advection Dominated Accretion Flow. In these conditions the flow is able to drive a strong matter outflow (e. g. Poutanen et al. 2007).

1.4.2 Spectral properties

Given that the majority of ULXs are likely to be X-ray binaries, a comparison of their X-ray spectral properties with those of known Galactic Black Hole

Binaries (BHBs) is appropriate. An extended treatment of these latter can be found in the exhaustive review of Remillard & McClintock (2006).

Spectral properties of Galactic BHBs In Galactic BHBs, we distinguish two components of the spectrum:

- a thermal component, generally modelled by a multicolour-blackbody spectrum with $T \sim 1\,\mathrm{keV}$;
- a high-energy component that is described by a power law $N(\mathcal{E}) \sim \mathcal{E}^{-\gamma}$.

The relative contribution of the two components changes with time, as discovered by Tananbaum et al. 1972. They observed a *transition* from a soft to the hard X-ray spectrum ($2 \div 6\,\mathrm{keV}$) in the X-ray binary Cyg X-1. That's why it is common to speak about *state* and *state transitions* in the X-ray spectra of BHBs. Often the power-law continuum of the X-ray spectrum of a Galactic BHBs shows a break or an exponential cut-off at high energies $\sim 60\,\mathrm{keV}$ (Remillard & McClintock 2006).

The soft state of the spectrum is typically dominated by the thermal component, and it is possible to observe it when the luminosity in the $2 \div 20\,\mathrm{keV}$ energy range is brighter (it is also called *high/soft state*); the hard state is generally described by a power law $\sim \mathcal{E}^{-\gamma}$ with spectral index $\gamma \sim 1.7$ (Remillard & McClintock 2006). We observe it when the source is fainter in the $2 \div 20\,\mathrm{keV}$ energy range (we also refer to it as *low/hard state*). A thorough characterization of the BHB-spectral states would also require an accurate analysis of the timing properties that is beyond the goals of this thesis. We mention only that a typical hallmark of some spectral states is presence of Quasi-Periodic Oscillations (QPOs), i. e. some quasi periodic variability in the power-density spectrum. Although they are a rather typical feature of accretion-powered emission spectra, QPOs provide an useful tool in the BHB-spectral classification because they seem to be somehow related to the transition between different states.

The study and classification of QPOs are based on some of their intrinsic parameters it is possible to observe, namely their mean frequency, width and associated noise (see Motta 2016); depending on the value of these parameters, it is possible to attempt a physical explanation for their origin. At least for those occuring at low frequencies, it is generally accepted that they originate from a general-relativistic effect[2] (see e. g. Motta 2016 and references therein).

QPOs can then be used for identifying another emission state of the BHB-spectra, called *very high state*: the very high state is indeed chatacterized by QPOs and high luminosity, with the X-ray spectrum showing a thermal component and a power law with a steep index ($\gamma \sim 2.5$) (Remillard & McClintock 2006).

Spectral properties of ULXs Even though BHB- and ULX-spectra show similarities, significant differences are found between them.

Similarly to BHBs, there is spectral variability between states (as in Fig. 1.2, Kubota et al. 2001) although the properties of these states are not so well defined. There are indeed some ULXs whose spectra are well described by a power-law, while other are better fitted with a multicolour blackbody disc (Fig. 1.2).

The better spectral resolution achieved e. g. by XMM-Newton shed light on the ULX spectra, highligthing differences from Galactic BHB-spectra. Many ULX spectra could be initially fitted with single-component models because of their poor spectral resolution. However, high counting statistics spectra taken later on showed that the X-ray spectral shape consists of two convex (thermal like) components one below 1 keV (soft component) and other at higher energies (often described phenomenologically with an optically thick Comptonizing component).

[2] I. e. the Lense-Thirring precession. For this reason QPOs can in principle be used also for determining the mass of the accretor compact object.

These spectral features cannot be fitted by the model of BHB spectra and suggest that they represent a new spectral state. This is usually referred to as *Ultraluminous state* (Gladstone et al. 2009; see Fig. 1.3) since it is observed only for luminosities $\gtrsim 10^{39}\,\mathrm{erg\,s^{-1}}$.

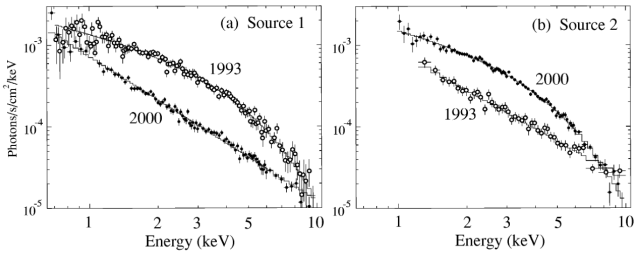

Figure 1.2: An example of transition between *spectral states* in two ULXs in the spiral galaxy I342 (Kubota et al. 2001). The X-ray spectra were obtained in two different *ASCA* observations.

1.4.3 Environment

ULXs are found in both elliptical and spiral galaxies (Feng & Soria 2011, Mushotzky 2004), but they are systematically brighter in spirals ($\mathcal{L}_{\mathrm{X,spirals}} \gtrsim 5\times10^{39}\,\mathrm{erg\,s^{-1}}$) than those hosted in ellipticals ($\mathcal{L}_{\mathrm{X,ellipticals}} \lesssim 2\times10^{39}\,\mathrm{erg\,s^{-1}}$).

Moreover, the number of ULXs in a given galaxy clearly correlates with its Star Formation Rate (SFR) (see Fig. 1.4; Mapelli et al. 2010, Mushotzky 2004). Actually the relation between the number of ULXs and SFR is probably dependent also on the metallicity of the stellar environment (Mapelli et al. 2010; Prestwich et al. 2013) where the stellar BH formed. As suggested by Zampieri & Roberts (2009), the metallicity of the progenitor star should affect the BH mass. While at solar metallicities the stellar envelope of a massive star is removed thanks to line-driven stellar winds, at lower metallicities the process is less effective, leaving a more massive star at the time of core collapse. This in

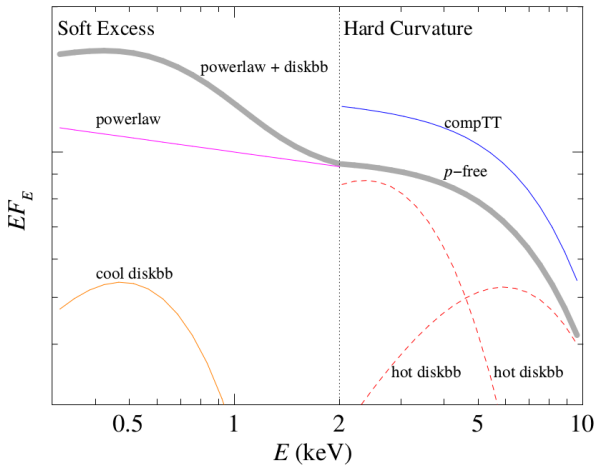

Figure 1.3: A typical behaviour of an ULX spectrum (grey solid line), where the various components are distinguishable (Feng & Soria 2011).

turn may cause most of the envelope to fallback after the supernova explosion or may induce the direct collapse of the star to a BH (of mass comparable to that of the final mass of the star; see Fig. 1.5.)

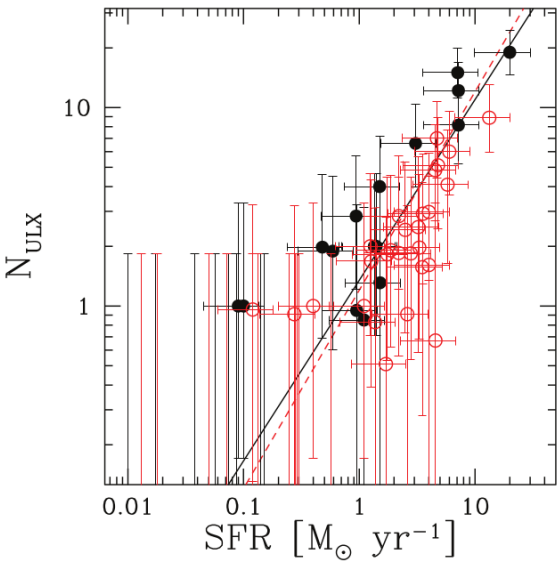

Figure 1.4: Positive correlation of the number of Massive stellar BHs $N_{\rm BH}$ with SFR (Mapelli et al. 2010).

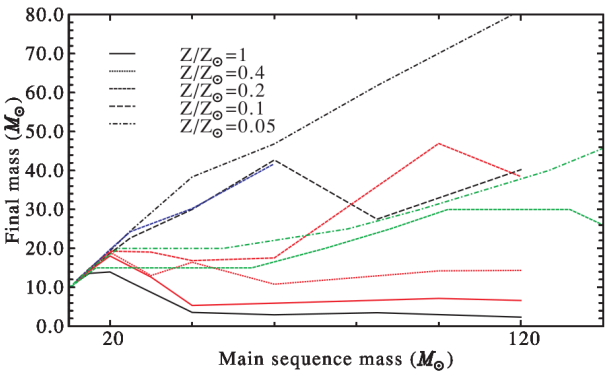

Figure 1.5: Theoretical dependence of the final mass of the star on its initial main sequence mass for different metallicities (Zampieri & Roberts 2009).

Chapter 2

ULX Pulsars

The main focus of this Thesis is studying the ULX Pulsars, interpreted as accreting Neutron Stars (NSs) endowed with a strong magnetic field B. Since the latter reduces significantly the Thomson opacity $k_{\rm T}$ (at least if $B > 12\,{\rm G}$), it contributes to enhance the total luminosity emitted by an accreting magnetized NS. In Sec. 2.1-2.3 we discuss in detail the physics of the accretion onto magnetized NSs, while Sec. 2.4 containes a summary of the main observational properties of the known ULX Pulsars.

2.1 Introduction

Until few years ago ULXs have always been modelled as accreting BHs as discussed in the previous Chapter. The discovery of a pulsing ULX in the nuclear region of the galaxy M82 (M82 X-2, Bachetti et al. 2014) and of two other pulsars thereafter (NGC 7793 P13, Israel et al. 2017a, Fürst et al. 2016; NGC 5907 X-1, Israel et al. 2017b) changed completely our view of ULX and forced us to consider accretion-powered pulsars as alternative model.

The physics of the accretion onto NSs is rather different from that required for modelling accretion onto BHs: NSs have a solid surface and are indeed known

to be *magnetized* stars, whose magnetic-field strenght B ranges between $10^8 \div 10^{15}$ G. In the following we will refer mainly to the case of highly magnetized-NSs (with $B \sim 10^{13} \div 10^{15}$ G): we will show that magnetic field in this interval may allow for the observed Super-Eddington luminosities.

Clearly we must take in account that the magnetic field plays a role in the interaction of radiation with matter: i. e. the electron scattering cross section differs from the Thomson cross section $\sigma_{\rm T}$.

We will carefully treat this aspect in the next chapter, when we will describe a recently-proposed model for NS ULXs. For the moment we concentrate on the basic phenomenology of accretion onto magnetized NSs.

2.2 Disc-fed accretion onto magnetized NSs

Suppose to deal as usual with a binary system, this time with a NS-accretor of radius R and mass M, and a donor star loosing matter through the inner Lagrangian Point L_1 and forming a thin accretion disc. As the stream of the accreting plasma approaches the NS-magnetosphere, the accretion disc is disrupted by the interaction with the magnetic field B. The radius at which this occurs is approximately where the raw pressure of the gas balances the magnetic pressure:

$$\frac{1}{2}\rho v(r)^2 = \frac{B(r)^2}{8\pi}\,. \tag{2.2.1}$$

Here:

- v is the bulk velocity of the gas, assumed for the sake of simplicity equal to the free-fall velocity $v_{\rm ff} = \sqrt{2GM/r}$ (of the same order of magnitude of the Keplerian velocity);
- ρ is the gas density (calculated from the continuity equation);
- $B(r)$ is the magnetic field, assumed to be dipolar $B(r) = \mu/r^3$, where $\mu = B^* R^3$ is the dipolar magnetic moment and B^* is the magnetic field

at the surface of the star.

Equation (2.2.1) can be solved for r and gives:

$$\mathcal{R}_{\rm A} = \dot{M}^{-2/7}(2GM)^{-1/7}\mu^{4/7}\,. \tag{2.2.2}$$

The radius $\mathcal{R}_{\rm A}$ is often referred to as **Alfvén radius**.

We stress the fact that this radius must be intended as a *scale lenght* that provides an order of magnitude estimate for the distance at which the magnetic field becomes dynamically important. A more rigorous calculation can be done by solving the whole set of MHD equations for the so-called *magnetospheric radius*[1] $R_{\rm M}$: for $r < R_{\rm M}$, the magnetic field becomes dynamically important and the accreting plasma will follow the magnetic-field lines (see Fig. 2.1).

2.2.1 Critical luminosity and accretion columns

We know that magnetic-field lines move close between them as they approach the NS-surface: since the accreting plasma is dynamically bound to magnetic-field lines it will accumulate in two funnell-shaped structures known as **accretion funnels**, at the base of which there are the magnetic polar caps.

Following the model developed by Basko & Sunyaev (1976), we assume that at a certain radius above the NS surface the flow will reach the sonic point, i. e. that its free-fall velocity will be equal to the sound speed of the gas. A shock will form if the luminosity (accretion rate) is above a certain value $\mathcal{L}^*$ ($\dot{M}^*$), e. g. given by Mushtukov et al. (2015a):

$$\mathcal{L}^* \simeq \frac{c}{k_{\rm eff}} l_0 \frac{GM}{R}\,, \tag{2.2.3}$$

where $k_{\rm eff}$ is the effective opacity and l_0 is the lenght of the circle representing the footprint of the accretion column on the NS surface (see Sec. 3.2). Hence two scenarios are possible:

[1] It is worth noting that magnetospheric radius preserves the same analytical dependence on the magnetic moment μ.

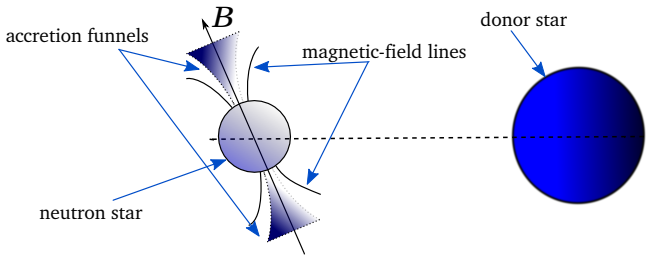

Figure 2.1: A sketch of the geometry of the accretion flow in a magnetizes NS: accreting matter flowing from the donor star follows the B-field lines and forms accretion funnels onto the NS surface.

- if $\mathcal{L} < \mathcal{L}^*$, no shock forms and accreting matter is stopped directly at the NS-surface, hence thermalizing and emitting X-rays;

- if $\mathcal{L} > \mathcal{L}^*$ a shock forms above the NS surface and accreting matter sinks in a so-called accretion column inside which it is gradually halted by the radiation pressure.

Since $\mathcal{L}^*$ is typically of the order of $10^{37}\,\mathrm{erg\,s^{-1}}$ we are mostly interested in the latter case, where the accretion column height can reach in principle the Alfvén radius $\mathcal{R}_\mathrm{A}$ for sufficiently high X-ray luminosities. Radiation is in large part emitted perpendicularly to the magnetic-field because electron scattering opacity is lower in that direction.[2]

The Rankine-Hugoniot jump-conditions written for a politropic equation of state $P \sim \rho^\Gamma$ between the pre-shock and the post-shock region (labelled with

[2]For high values of the magnetic-field strenght ($B \gtrsim 10^{12}\,\mathrm{G}$), but we will go deeper in detail in Sec. 3.4.3.

subscripts 1 and 2, respectively) are:

$$\rho_1 u_1 = \rho_2 u_2 \qquad \text{conservation of mass} \qquad (2.2.4)$$

$$P_1 + \rho_1 u_1^2 = P_2 + \rho_2 u_2^2 \qquad \text{conservation of momentum} \qquad (2.2.5)$$

$$\frac{1}{2}u_1^2 + \frac{\Gamma}{\Gamma - 1}\frac{P_1}{\rho_1} = \frac{1}{2}u_2^2 + \frac{\Gamma}{\Gamma - 1}\frac{P_2}{\rho_2} \qquad \text{conservation of energy} \qquad (2.2.6)$$

From them it is possible to obtain an expression for the post-shock velocity[3]:

$$u_2 = \frac{\Gamma - 1}{\Gamma + 1} u_1 \,, \qquad (2.2.7)$$

that, for a radiation-dominated gas ($\Gamma = 4/3$) returns

$$u_2 = \frac{u_1}{7} \,. \qquad (2.2.8)$$

Assuming as before that the accreting gas falls in the NS-gravitational field with free-fall velocity, the post-shock velocity in the sinking region will be then

$$v = \frac{v_{\rm ff}}{7} \,. \qquad (2.2.9)$$

This latter condition will be used extensively in our model.

2.3 Effects preventing accretion

In this Section we focus on the conditions under which accretion onto a magnetized NS can take place.

2.3.1 Propeller effect

We know that the accreting plasma is expected to have a high angular momentum, but we also expect that a particle must get rid of a part of it for settling on a smaller orbit until it reaches the NS surface. In the typical case of

[3]We are obviously considering the simple case in which Mach number is formally infinite, the so-called *strong shock*: equations (2.2.4-2.2.6) would eventually return for $\Gamma = 5/3$ the result of the gasdynamics for an ideal gas.

an accretion disc around a BH the loss of angular momentum is typically caused by the viscous torques; for an accreting NS, we must take in account also the magnetic field.

We start considering an important parameter:

$$\omega_s = \frac{\Omega_s}{\Omega_{\rm K}(\mathcal{R}_{\rm A})}\,, \tag{2.3.1}$$

where Ω_s is the angular velocity of the NS and $\Omega_{\rm K}(\mathcal{R}_{\rm A})$ is the keplerian angular velocity evaluated at the Alfvén Radius. ω_s is generally called *fastness parameter*.

It is possible to show that the total torque N (including material, magnetic, and viscous stresses) can be written as:

$$N = n(\omega_s) N_0\,, \tag{2.3.2}$$

where $n(\omega_s)$ is often referred to as *adimensional accretion torque*, and depends only on ω_s. N_0 (the torque of the accreting matter) is given by:

$$N_0 = \frac{\rm d}{{\rm d}t}[M(t) r_1^2 \Omega] \simeq \rho v r_1^2 \Omega S_1\,. \tag{2.3.3}$$

A detalied modelling of $n(\omega_s)$ is needed for investigating the spin properties of a rotating NS: the term N_0 causes a spin-up of the NS, since it accounts for the angular momentum transferred by the accreting plasma, while the other contributions to the torque (magnetic and viscous stresses) eventually present can either spin up or spin down the NS[4]. They are accounted for by the expression of $n(\omega_s)$.

A simple analytic expression for $n(\omega_s)$ is[5] (Ghosh 2002):

$$n(\omega_s) = 1 + \frac{1}{2(1-\omega_s)}\,. \tag{2.3.4}$$

[4] In the case of a magnetized NS the sign of the torque depends on the so-called *azimuthal pitch* $\gamma_\phi = B_\phi / B_z|_{z=-h}$, where h is the height of the disc (see Ghosh & Lamb 1979, III), whose sign can change.

[5] Alternative expressions can also be found in e. g. Dall'Osso et al. (2015).

From equations (2.3.4, 2.3.2) it turns out that accretion is possible (the torque is positive) if:

$$\omega_s < 1\,. \tag{2.3.5}$$

From equation (2.3.1) we are indeed requiring that the whole magnetosphere rotates with an angular velocity lower than that of the accreting gas: the condition (2.3.5) can be rewritten as:

$$\mathcal{R}_{\rm A} < R_{\rm C}\,, \tag{2.3.6}$$

where $R_{\rm C}$ is the *corotation radius*, namely the distance at which the Keplerian angular velocity equals the rotational angular velocity of the NS, in formulae $\Omega_s(R_{\rm C}) = \Omega_{\rm K}(R_{\rm C})$.

If $\mathcal{R}_{\rm A} > R_{\rm C}$ the NS cannot accrete since the NS rotational velocity is too high and centrifugal forces would then prevent matter from falling on it. This is the so-called **propeller effect** that fixes a requirement for the accretion onto a magnetized NS to take place.

Finally, the torques exterted on an accreting NS permit to estimate the mass-accretion rate $\dot{M}$ via the measured period derivative $\dot{P}$ (once an estimate for the value of B is provided). From equation (2.3.3), and using the continuity equation it is possible to show that:

$$\dot{M}\sqrt{GM\mathcal{R}_{\rm A}} = -2\pi I\frac{\dot{P}}{P}\,, \tag{2.3.7}$$

where I is the moment of inertia and we have written $\mathrm{d}L/\mathrm{d}t = -2\pi I\dot{P}/P$ ($L = I\Omega_s = 2\pi I/P$ is the NS angular momentum).

2.3.2 Thick disc

A fundamental assumption made in Sec. 2.2 is that the stream of plasma that is accreting onto the NS lies on the orbital plane, forming thus a *thin accretion disc* (Shakura & Sunyaev 1973); i. e. we are assuming that the disc-scale height $H(R)$ is much lower than the radius of the disc R.

If instead $H \sim R$ the disc becomes geometrically *thick* and advection of matter and energy take place allowing accretion above the Eddington limit (Abramowicz et al. 1988, Watarai et al. 2001). Radiation pressure may accelerate matter producing a powerful equatorial outflow (e. g. Poutanen et al. 2007). The radius at which advection energy starts to dominate is called *spherization radius* $R_{\rm sp}$ (Shakura & Sunyaev 1973).

$$R_{\rm sp} = R_{\rm M}\,. \tag{2.3.8}$$

If $R_{\rm sp} < R_{\rm M} < R_{\rm C}$ accretion is possible and the thin disc approximation still holds; if $R_{\rm sp} > R_{\rm M}$ and $R_{\rm M} < R_{\rm C}$ a strong plasma outflow develops and the NS accretes from a thick disc that would rapidly engulf the magnetosphere.

2.4 Observations of ULX Pulsar

A self-consistent model that accounts for all the observational properties of ULX pulsars is still missing. Here we summarize all the available data for the three known sources of this type.

2.4.1 M82X-2 (NuSTAR J095551+6940.8)

The starbust galaxy M82 is known to harbour a population of ULXs (Matsumoto et al. 2001) in its nuclear region. The two brightest among them, called M82X-1 and M82X-2 can be resolved only by means of the Chandra X-ray telescope because of their small angular separation of roughly 5 arcsec. The same area of the sky was targeted also by NuSTAR seven times between the 23rd January 2014 and the 6th March 2014; a careful analysis of the NuSTAR data (Bachetti et al. 2014) led to indentification of NuSTAR J095551+6940.8 with M82X-2 and revealed the presence of coherent pulsations. The observed period is $P \sim 1.37\,\mathrm{s}$, with an orbital modulation of 2.53 days (see Fig. 2.2), and its first-time derivative is $\dot{P} \sim -2 \times 10^{10}\,\mathrm{s\,s^{-1}}$. The X-ray luminosity reaches

$\mathcal{L}_{\rm X} \sim 1.8 \times 10^{40}\,{\rm erg\,s^{-1}}$, hence largely exceeding the Eddington limit for a BH with mass $M = 10\,{\rm M}_{\odot}$. The torque $N_0 \simeq 6 \times 10^{45} I_{45}\,{\rm gr\,cm^2\,s^{-1}}$ (2.3.7) implies a

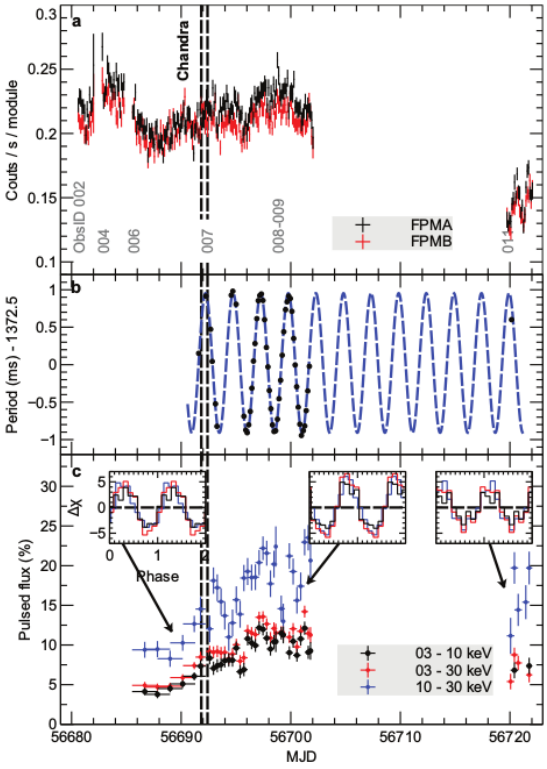

Figure 2.2: Panel *a*: lightcurves taken in the 3-30 keV energy band within 70" from the position of J095551+6940.8; different colours correspond to a different count rate. Panel *b*: measurements of the pulse period (black points) fitted with a sinusoidal ephemeris (blue dashed line) showing a $\sim$ 2.5 days modulation. Panel *c*: pulsed flux normalized to the total emission within 70" from the position of J095551+6940.8. The panels show the pulse profiles (Bachetti et al. 2014).

high value of the mass-accretion rate[6] $\dot{M}$, hence suggesting a disc-fed accretion

[6]In the assumption that it is entirely due to the matter torque N_0.

via Roche-lobe overflow; the presence of the coherent flux pulsations leads one to identify M82X-2 as an accreting NS.

2.4.2 NGC 7793 P13

The ULX P13 in the spiral galaxy NGC 7793 was observed several times since the first *Einstein* satellite observations carried out in 1979; subsequent observations with *ROSAT* (1992) and *Chandra* (2003) confirmed the presence of an ULX whose Eddington luminosity reaches $\sim 4 \times 10^{39}\,\mathrm{erg\,s^{-1}}$ (Motch et al. 2014). Optical measurements led to constrain the mass of the compact object in this source, that was determined to be $> 15\,\mathrm{M_\odot}$ (Motch et al. 2014). Recently (see Israel et al. 2017a and Fürst et al. 2016) detected a $\sim 0.42\,\mathrm{s}$ pulsation in the XMM Newton EPIC data of this source, showing that it contains a NS (see Fig. 2.3).

Albeit its luminosity is not as high as NGC 5907 ULX, the interpetation of the ULX P13 is non trivial. It is difficult to find a value of the magnetic field that, given the observed period P and its time-variation $\dot{P}$, fulfills all the requirements mentioned in the previous Section. An even more extreme case in this sense is represented by the ULX pulsar recently discovered, NGC 5907 ULX-1 (Israel et al. 2017b).

2.4.3 The case of NGC 5907 ULX-1

NGC 5907 ULX-1 is the most powerful ULX pulsar ever discovered at the present date. As its name already suggests, it was found in the spiral galaxy NGC 5907 with NuSTAR and with XMM Newton in 2003 (Israel et al. 2017b).

The observed luminosity is exceptionally high, reaching $0.25 \div 2 \times 10^{41}\,\mathrm{erg\,s^{-1}}$ (Israel et al. 2017b).

We summarize the main observational parameters for NGC 5907 ULX-1 in the Tab. 2.4.3. From Tab. 2.4.3 NGC 5907 ULX has also a suprinsingly

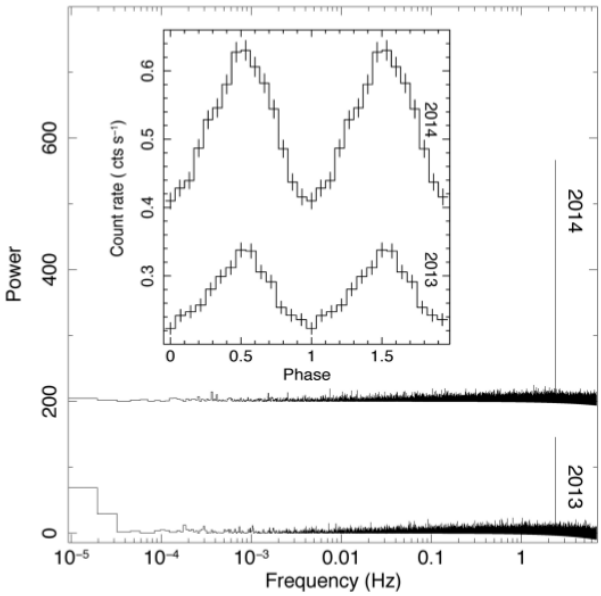

Figure 2.3: Folded lightcurve (*upper panel*) and Fourier power spectra taken in 2013 and 2014 of NGC 7793 P13. A pulsation is clearly detected with a frequency corresponding to $\sim 0.42\,\mathrm{s}$ (Israel et al. 2017a).

NGC 5907 ULX-1		
Luminosity $\mathcal{L}$	.....	$0.25 \div 2 \times 10^{41}\,\mathrm{erg\,s^{-1}}$
Period P (2003)	.....	$1.428\,\mathrm{s}$
Period P (2014)	.....	$1.136\,\mathrm{s}$

Table 2.1: Table summarizing the main observational parameters of NGC 5907 ULX-1 (Israel et al. 2017b).

high average value of $\dot{P}$: considering the eleven-years span between the two measurements, it is:

$$\dot{P} \sim (1.136\,\mathrm{s} - 1.428\,\mathrm{s})/11\,\mathrm{yr} \simeq -8.42 \times 10^{-10}\,\mathrm{s\,s^{-1}} \tag{2.4.1}$$

showing via equation (2.3.7) that the torque is very high: it is then likely that the donor star is filling its Roche Lobe.

A possible explanation of the luminosity of NGC 5907 ULX-1 is that the accreting NS is endowed with a multipolar magnetic field. As suggested by Israel et al. (2017b), a dipolar componet $B_1 = (0.2 - 3) \times 10^{13}\,\mathrm{G}$ and a multipolar component $B_2 = (0.7 - 3) \times 10^{14}\,\mathrm{G}$ can account for the observed luminosity of this ULX Pulsar (see Fig. 2.4).

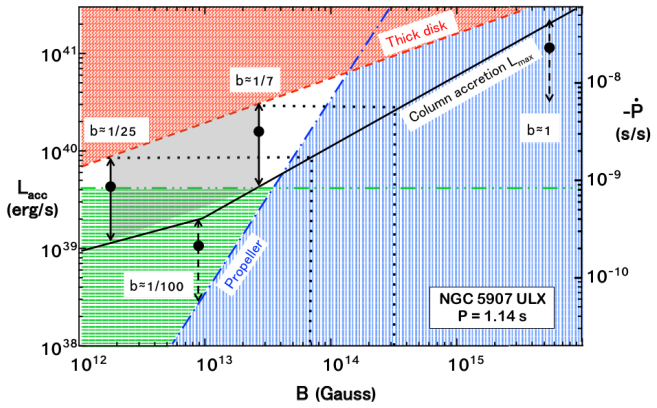

Figure 2.4: Luminosity of a ULX Pulsar versus magnetic field strenght. The region above the red dashed line corresponds to the case in which high geometrical thickness leads to a nearly spherical accretion (see Sec. 2.3). On the right of the blue dashed line, the propeller effect does not permit accretion. The green dashed line represents the minimum luminosity that can account for the observed $\dot{P}$ of NGC 5907 ULX-1. The arrows represent the interval of luminosity covered by the detected flux variations, where the black points represent the average luminosity; each arrow is labelled with the value of the beaming factor required to account for the observed flux, in order to not to imply a too high magnetic field.

Chapter 3

The model

This Chapter deals with the calculation of the accretion luminosity of a magnetized NS following the model proposed by Mushtukov et al. (2015b). Sec. 3.2 briefly presents the seminal treatment of Basko & Sunyaev (1976), on which the model of Mushtukov et al. (2015b) is based; in Sec. 3.3-3.5 we describe our implementation of the model and the iterative procedure of Mushtukov et al. (2015b), incorporated in the numerical (`FORTRAN90`) code `MACHD`; in Sec. 3.6 we present the results of our numerical computation and compare them with those of Mushtukov et al. (2015b).

3.1 Introduction

We calculate the maximum accretion luminosity of a magnetized NS using the approach introduced by Mushtukov et al. (2015b). The latter is based on the treatment published in Basko & Sunyaev (1976). The crucial improvement on the model of Mushtukov with respect to the treatment of Basko & Sunyaev is the inclusion of the correct dependence of the photon cross section on the

B-field[1].

As already mentioned before, accreting matter is first halted by the radiation-dominated shock, and then enters in the sinking region where it is stopped at the NS-surface. Very large luminosities are produced in the radiation-dominated plasma in this zone. The implementation of the model is done by means of a numerical code written in `FORTRAN90`.

3.2 Geometry of the accretion column

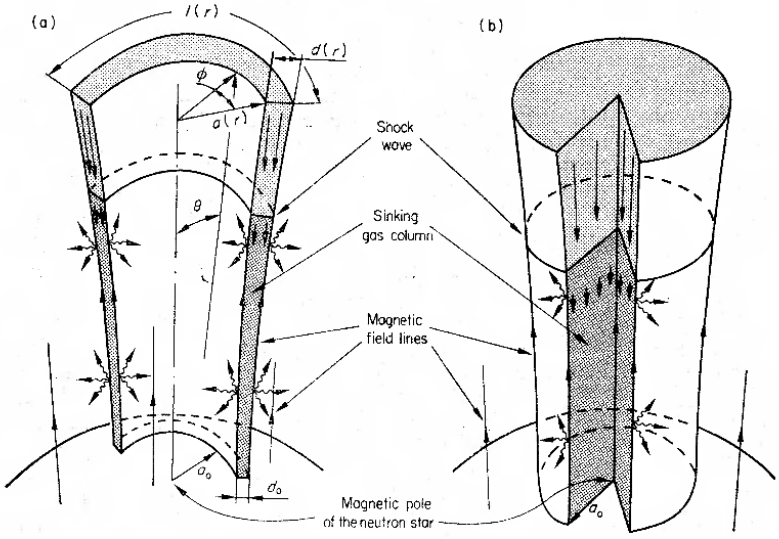

Figure 3.1: The two possible geometries of the accretion column, from Basko & Sunyaev (1976).

The geometry of the accretion column depends on whether:

- matter is accreted through an accretion disc formed in a Roche potential and arranges itself on a narrow wall of the column (Fig. 3.1, left);

[1]In Basko & Sunyaev the Thomson-cross section $\sigma_{\rm T}$ was adopted. They discussed the fact that high values of B may lower significantly its value (see Basko & Sunyaev 1976 for further details).

- matter flows on the NS surface via spherical accretion, filling then the whole column (Fig. 3.1, right).

In both cases the accreting plasma will cross a shock experiencing a deceleration. The relevant geometry considered in the following is that for an accretion disc. As shown in Fig. 3.1 left, we will use the following parameters to describe the geometrical configuration of the accretion column:

- the outer lenght of the accretion column, l_h;
- the thickness of the accretion column, d_h;
- the radius of the accretion column, a_h.

All these quantities vary with the height below the shock surface $h \in [0, H_x]$ (see Fig. 3.2).

The shape of the shock surface is shown in Fig. 3.2 (it will be discussed later).

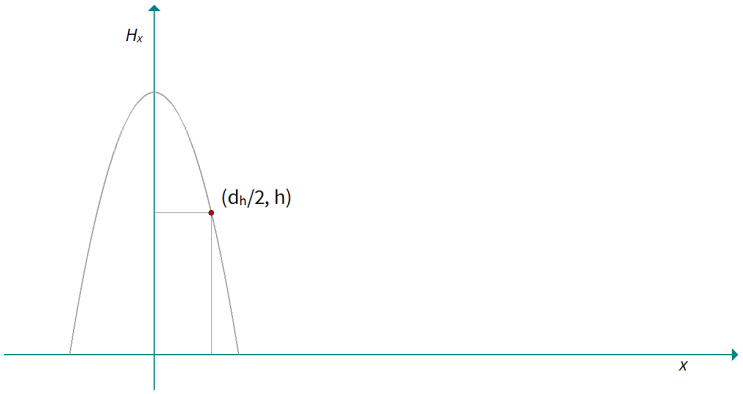

Figure 3.2: Profile of the shock surface, in a plane perpendicular to it. H_x is the height of the shock above the NS surface, while x and h are two coordinates across and along the accretion column.

3.3 Fundamental equations

As the accreting plasma approaches the Alfvén radius $\mathcal{R}_{\rm A}$, the ram pressure of the flow becomes of the same order of the magnetic pressure:

$$P_{\rm mag} = \frac{B^2}{8\pi} \tag{3.3.1}$$

As mentioned earlier, at this radius the magnetic field becomes dynamically important and channels the plasma along the magnetic-field lines until it reaches the shock surface with roughly free-fall velocity:

$$v_{\rm ff} = \sqrt{\frac{GM}{R + H_x}} \tag{3.3.2}$$

The model of Mushtukov et al. (2015b) is based on three equations, derived from the fundamental laws of thermodynamics and fluid dynamics. The main assumptions of the model are:

1. radiation balances the gravitational forces in the accretion column, i. e. the infalling plasma is in **hydrostatic equilibrium**;
2. matter falling in the accretion column is **optically thick** and in **local thermodynamic equilibrium** with radiation;
3. radiation transport across the column can treated in the **plane-parallel diffusion approximation**.

Hydrostatic equilibrium We assume that radiation pressure dominates and hydrostatic equilibrium along the accretion column is expressed as:

$$\frac{\partial P_{\rm rad}(x,h)}{\partial h} = -\rho \frac{GM}{(R+h)^2}\,, \tag{3.3.3}$$

where ρ is the matter density and $P_{\rm rad}(x,h)$ is the radiation pressure.

A general solution of the equation (3.3.3) is then given by:

$$P_{\rm rad}(x,h) = P_{\rm rad}(x,H_x) + \int_h^{H_x} \rho \frac{GM}{(R+y)^2}\,{\rm d}y\,. \tag{3.3.4}$$

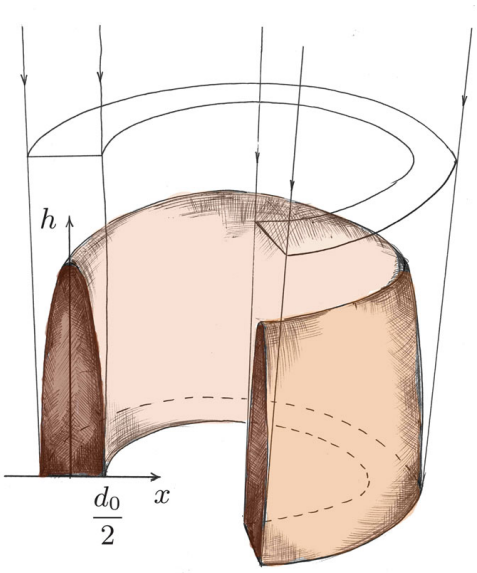

Figure 3.3: Accretion-column geometry (Mushtukov et al. 2015b).

Local thermodynamic equilibrium The equation of radiative transfer fixes the budget with which the intensity of a beam of radiation I_ν varies when it interacts with matter. Though its general solution is difficult to calculate, a good approximation for our goals can be provided complying with the hypotheses of high optical thickness and local thermodynamic equilibrium, for which the solution of the equation of radiative transfer writes:

$$I_\nu = \mathcal{B}_\nu(T)\,, \tag{3.3.5}$$

where $\mathcal{B}_\nu(T)$ is the Planck function. Since the infinitesimal radiation pressure $\mathrm{d}P_{\mathrm{rad}}$ of a single radiation beam with momentum $\mathbf{k}$ passing through an infinitesimal oriented surface and emitted within a solid angle $\mathrm{d}\Omega$ in a frequency band $\mathrm{d}\nu$ is by definition:

$$\mathrm{d}P_{\mathrm{rad}} = \mu^2 I_\nu \,\mathrm{d}\Omega\,\mathrm{d}\nu \tag{3.3.6}$$

(where μ is the cosine of the angle between $\mathbf{k}$ and the normal to the surface), the integration of the equation (3.3.6) combined with the equation (3.3.5) gives:

$$P_{\rm rad} \simeq \frac{\epsilon_{\rm R}}{3} = \frac{aT^4}{3}\,, \tag{3.3.7}$$

where $a = 7.5646 \times 10^{-15}\,{\rm erg\,cm^{-3}\,K^{-4}}$ is the radiation density constant.

Radiative transfer Assuming plane-parallel diffusion approximation in the x direction, the first moment of the radiative transfer equation takes the form:

$$\frac{\partial P_{\rm rad}(x,h)}{\partial x} = -\rho k_\perp \frac{\mathcal{F}_\perp(x,h)}{c}\,, \tag{3.3.8}$$

where $k_\perp$ is the Rosseland-mean opacity and $\mathcal{F}_\perp(x,h)$ the radiation flux across the accretion column.

We can integrate equation (3.3.8) between x and $d_h/2$ to get:

$$P_{\rm rad}(x,h) = P_{\rm rad}\left(\frac{d_h}{2},h\right) + \frac{1}{c}\int_x^{d_h/2} \rho k_\perp \mathcal{F}_\perp(x,h)\,{\rm d}x\,. \tag{3.3.9}$$

3.4 The model of Mushtukov et al.

In the previous paragraphs we discussed the assumptions and wrote the three main equations of the model; for the sake of clarity they are summarized in this

box:

MAIN EQUATIONS OF THE MODEL

HYDROSTATIC EQUILIBRIUM

$$P_{\rm rad}(x,h) = P_{\rm rad}(x,H_x) + \int_h^{H_x} \rho \frac{GM}{(R+y)^2}\,{\rm d}y \qquad (3.3.4)$$

LOCAL THERMODYNAMIC EQUILIBRIUM

$$P_{\rm rad} = \frac{aT^4}{3} \qquad (3.3.7)$$

RADIATIVE TRANSFER

$$P_{\rm rad}(x,h) = P_{\rm rad}\left(\frac{d_h}{2},h\right) + \frac{1}{c}\int_x^{d_h/2} \rho k_\perp \mathcal{F}_\perp(x,h)\,{\rm d}x \qquad (3.3.9)$$

3.4.1 Analytical estimates

In order to obtain order-of-magnitude estimates for the considered physical quantities[2], let us simplify even more the treatment with some additional assumptions that we will relax afterwards.

Let us then assume that the density ρ is constant and that the flux along the direction perpendicular to the magnetic-field lines $\mathcal{F}_\perp(x,h)$ can be expressed as[3]:

$$\mathcal{F}_\perp(x,h) \simeq \mathcal{F}_{\perp,{\rm esc}}(h)\frac{2x}{d_0}\,. \qquad (3.4.1)$$

If we neglect also the radiation pressure at $x = d_0/2$ ($P_{\rm rad}(d_0/2,h) = 0$), equation (3.3.9) returns:

$$P_{\rm rad}(x,h) \sim \frac{\tau_0 \mathcal{F}_{\perp,{\rm esc}}(h)}{4c}\left(1 - \frac{4x^2}{d_0^2}\right)\,, \qquad (3.4.2)$$

where we have introduced the optical depth across the accretion column $\tau_0 =$

[2]We will use these estimates as initial guess in numerical calculations.

[3]We will not relax this assumption later.

$\rho k_\perp d_0$; equation (3.4.2) is our first tool to constrain the escaping flux $\mathcal{F}_{\perp,\mathrm{esc}}$:

$$\mathcal{F}_{\perp,\mathrm{esc}}(h) = \frac{4c}{\tau_0} P_{\mathrm{rad}}(0,h) \tag{3.4.3}$$

Assuming that $P_{\mathrm{rad}}(0,H_0)$ can be neglected, we obtain $P_{\mathrm{rad}}(0,h)$ from equation (3.3.4):

$$P_{\mathrm{rad}}(0,h) \sim \rho \frac{GM}{R+H_0} \frac{H_0-h}{R+h}\,. \tag{3.4.4}$$

From equations (3.4.3, 3.4.4) we then obtain:

$$\mathcal{F}_{\perp,\mathrm{esc}}(h) \simeq \frac{4cP_{\mathrm{rad}}(0,h)}{\tau_0} = \frac{4c}{k_\perp d_0} \frac{GM}{R+H_0} \frac{H_0-h}{R+h}\,. \tag{3.4.5}$$

Evaluating thus equation (3.4.5) for $h=0$ and then substituting it in equation (3.4.2), $P_{\mathrm{rad}}(x,0)$ can be expressed as:

$$P_{\mathrm{rad}}(x,0) \simeq \rho \frac{GM}{RH_x} \tag{3.4.6}$$

where H_x is defined by the following expression:

$$\frac{H_x}{H_x+R} = \frac{H_0}{R+H_0}\left(1-\frac{4x^2}{d_0^2}\right) \tag{3.4.7}$$

or explicitely:

$$H_x = \frac{RH_0\left(1-4x^2/d_0^2\right)}{R+H_0(4x^2/d_0^2)}\,. \tag{3.4.8}$$

This expression shows that, for small accretion-column heights $H_0 \ll R$, the accretion shock surface has roughly a parabolic shape, as already anticipated:

$$\frac{H_x}{H_0} \simeq (1-\eta_x^2)\left(1-\frac{H_0}{R}\eta_x^2\right) \sim 1-\left(1+\frac{H_0}{R}\right)\eta_x^2 \quad \text{if } \eta_x \ll 1\,, \tag{3.4.9}$$

where $\eta_x \equiv 2x/d_0$.

From the expression of $\mathcal{F}_{\perp,\mathrm{esc}}$ we can immediatly obtain the total luminosity $\mathcal{L}$ emitted by the accretion column, integrating over the emitting surface (the wall of the accretion column):

$$\mathcal{L} = 4l_0 \int_0^{H_0} \mathcal{F}_{\perp,\mathrm{esc}}(h)\,\mathrm{d}h = 16GMf\left(\frac{H_0}{R}\right)\frac{l_0}{d_0}\frac{c}{k_\perp}\,, \tag{3.4.10}$$

where

$$f\left(\frac{H_0}{R}\right) \equiv \log\left(1+\frac{H_0}{R}\right) - \frac{H_0}{R+H_0}\,. \tag{3.4.11}$$

For $\mathcal{L} \sim 10^{39}\,\mathrm{erg\,s^{-1}}$ and assuming $k_\perp \sim k_\mathrm{T}$, it is $H_0 \sim 0.75R$. We will use this value of the height as initial guess in our iterative numerical scheme.

In the following we will relax some of the simplifying assumptions introduced in this Section.

3.4.2 Velocity and density across the column

In order to obtain more accurate results it is worth replacing the assumption $\rho = \text{const}$ with a more realistic density-profile. Here we calculate ρ from the *equation of continuity* in fluid dynamics:

$$\frac{\partial\rho}{\partial t} + \nabla\cdot(\rho\mathbf{v}) = 0 \tag{3.4.12}$$

that, under stationary conditions, reduces to:

$$\rho v = \frac{\dot{M}}{2S_\mathrm{D}}\,, \tag{3.4.13}$$

where v is the velocity of the accreting gas, $\dot{M}$ is the mass-accretion rate and S_D is the footprint of the accretion column[4]. The velocity profile can be found by solving the whole set of HD-equations (see for instance Wang & Frank 1981); one can show that has a power-law behaviour:

$$v \sim h^\xi \tag{3.4.14}$$

(see Mushtukov et al. 2015b). The exponent ξ is in the range $1 \div 5$ and tends to increase for high values of the ratio[5] H_0/R; Mushtukov et al. (2015b) discuss the effects of different values of ξ on the solution and find that $\xi = 1$ is a good choice.

[4] Hence the factor 2 at the denominator.

[5] More precisely the actual value of ξ depends on both opacity and thickness variations along the magnetic-field lines and on the magnetic-field structure.

Recalling that the post-shock velocity is initially $\sim v_{\rm ff}/7$ (see Sec. 2.2), we assume:

$$v(x,h) = v_{\rm ff}(x)\frac{h}{7H_x}\,. \tag{3.4.15}$$

Substituing in (3.4.13) and solving for ρ we obtain:

$$\rho(x,h) = \rho_{\rm ff}(x)\left(\frac{h}{7H_x}\right)^{-1}\,, \tag{3.4.16}$$

where, using equation (3.4.13) we define the *free-fall density* $\rho_{\rm ff}$ as:

$$\rho_{\rm ff}(x) = \frac{\dot{M}}{2S_{\rm D}v_{\rm ff}(x)}\,. \tag{3.4.17}$$

3.4.3 Magnetized Thomson scattering cross section

As it can be seen from equations (1.2.2, 3.3.9), opacity is another crucial quantity of the model that has to be properly treated.

The electron-scattering cross section $\sigma_{\rm T}$ for a non-relativistic plasma in absence of a strong magnetic field is given by the Thomson forumla:

$$\sigma_{\rm T} = \frac{e^4}{6\pi m_e^2 c^4}\,. \tag{3.4.18}$$

However in presence of high magnetic fields, as we are considering, the cross section has a complicate expression. Its thorough derivation requires a full-Quantum ElectroDynamics (QED) calculation which is beyond the goals of the present work. In the following we briefly introduce the physical framework and then summarize the results (for further details see e. g. Canuto et al. 1971, Herold 1979, Paczyński 1992, Taverna & Turolla 2017).

We know from basic Physics that the energy radiated per unit time along the direction θ within a solid angle $\mathrm{d}\Omega$ by an accelerated charged particle (e. g. an electron) is given by:

$$-\frac{\mathrm{d}\mathcal{E}}{\mathrm{d}t}\mathrm{d}\Omega = \frac{|\ddot{\mathbf{p}}|\sin^2\theta}{16\pi^2c^3}\mathrm{d}\Omega\,, \tag{3.4.19}$$

where $\ddot{\mathbf{p}}$ is the second-time derivative of the electric dipole moment $\mathbf{p} = -e\mathbf{r}$, with $\mathbf{r} = (x\hat{\mathbf{i}}_x + y\hat{\mathbf{i}}_y)$. Integration of equation (3.4.19) over the solid angle Ω

returns the well-known *Larmor formula*. If the acceleration $\mathbf{a} = \ddot{\mathbf{r}}$ experienced by the electron is caused by an oscillating electrical field $\mathbf{E}(t) = (E_{0,x}\hat{\mathbf{i}}_x + E_{0,y}\hat{\mathbf{i}}_y)e^{i\omega t}$ of an incident electromagnetic wave, we obtain the classical *Thomson scattering* power and cross section, as summarized below. The force associated to $\mathbf{E}(t)$ is:

$$\mathbf{F}(t) = m_e\ddot{\mathbf{r}} = -e\mathbf{E}(t)\,, \tag{3.4.20}$$

from which the second-time derivative of the dipole moment follows immediately. Averaging[6] all the directions $\hat{\mathbf{i}}_x$ and $\hat{\mathbf{i}}_y$, equation (3.4.19) can be rewritten as:

$$-\frac{\mathrm{d}\mathcal{E}}{\mathrm{d}t}\mathrm{d}\Omega = \frac{\mathrm{d}\sigma_\mathrm{T}}{\mathrm{d}\Omega}\frac{S}{2}\mathrm{d}\Omega \tag{3.4.21}$$

where we introduced the differential cross section $\mathrm{d}\sigma_\mathrm{T}/\mathrm{d}\Omega$ with the following meaning:

$$\frac{\mathrm{d}\sigma}{\mathrm{d}\Omega} = \frac{\text{energy radiated per unit time per solid angle}}{\text{incident energy per unit time per unit area}} \tag{3.4.22}$$

or:

$$\frac{\mathrm{d}\sigma}{\mathrm{d}\Omega} = \frac{1}{\langle S\rangle}\left\langle\frac{\mathrm{d}P}{\mathrm{d}\Omega}\right\rangle\,. \tag{3.4.23}$$

S is the average Poynting vector and P is the power. In the case of Thomson scattering it is:

$$\frac{\mathrm{d}\sigma_\mathrm{T}}{\mathrm{d}\Omega} = \frac{3}{16\pi}\sigma_\mathrm{T}(1+\sin^2\theta)\,. \tag{3.4.24}$$

Let us now come back to the case of interest, in which a strong magnetic field can significantly affect the interaction of radiation with matter. Equation (3.4.23) becomes more complex (see e. g. Canuto et al. 1971), since one has to replace the electric force given in equation (3.4.20) with the expression of the Lorentz force:

$$\mathbf{F}(t) = -e\left(\mathbf{E}(t) + \frac{1}{c}\mathbf{v}\times\mathbf{B}\right)\,. \tag{3.4.25}$$

Using this expression to calculate $\ddot{\mathbf{p}}$ and inserting it in equation (3.4.19), we obtain the istantaneous energy emitted per unit time in an infitesimal solid angle

[6]This is commonly done by making use of the Poynting's theorem, as in Rybicky & Lightman (2004).

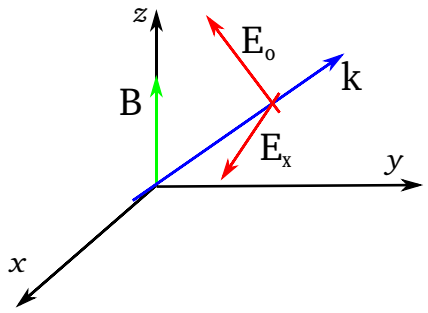

Figure 3.4: Polarization states of the photons with momentum **k** (blue arrow) in the case of a strong magnetic field **B** (green arrow): photons may be either in the X-mode ($\mathbf{E}_\mathrm{X}$, whose direction is perpendicular to the **B**-**k** plane) or in the O-state ($\mathbf{E}_\mathrm{O}$, whose direction is parallel to the **B**-**k** plane).

for radiation, that for high magnetic-field strenghts requires a QED approach (see e. g. equation 16 and Appendix A, B in Canuto et al. 1971).

It is possible to show that the cross section depends on:

- the magnetic-field strenght;
- the polarization state of both the incident and the scattered photon, that can be either parallel or perpendicular to the B-field direction respectively, referred to as *ordinary* (O) and *extraordinary* (X) mode (see Fig. 3.4);
- the angle θ between the photon momentum **k** and the magnetic-field direction.

In the case of high magnetic-field strenghts, we expect a swapping of the polarization mode O in mode X as pointed out in e. g. Mushtukov et al. (2012): for the sake of simplicity we will then consider only X-polarized photons, that after

the scattering may have either X or O polarization.

Let us then consider an *incoming* photon with momentum $\mathbf{k}$ moving within an infinitesimal solid angle $\mathrm{d}\Omega = \sin\theta \mathrm{d}\theta\mathrm{d}\phi$; the *outcoming* photon will be scattered within the solid angle $\mathrm{d}\Omega' = \sin\theta'\mathrm{d}\theta'\mathrm{d}\phi'$ in the same frame of reference. The two contributions to the differential cross section are (see Taverna & Turolla 2017), for $\mathcal{E} \ll \mathcal{E}_{\mathrm{Cycl}}$:

$$\frac{\mathrm{d}\sigma_{\mathrm{X}\to\mathrm{O}}}{\mathrm{d}\Omega'} = \sigma_{\mathrm{T}}\frac{3}{8\pi}\left(\frac{\mathcal{E}}{\mathcal{E}_{\mathrm{Cyc}}}\right)^2 \mu'^2\cos^2(\phi-\phi') \tag{3.4.26}$$

$$\frac{\mathrm{d}\sigma_{\mathrm{X}\to\mathrm{X}}}{\mathrm{d}\Omega'} = \sigma_{\mathrm{T}}\frac{3}{8\pi}\left(\frac{\mathcal{E}}{\mathcal{E}_{\mathrm{Cyc}}}\right)^2 \sin^2(\phi-\phi')\,, \tag{3.4.27}$$

where we have imposed $\mu' = \cos\theta'$. The total differential cross section is then:

$$\frac{\mathrm{d}\sigma_{\mathrm{X}}}{\mathrm{d}\Omega'} = \frac{\mathrm{d}\sigma_{\mathrm{X}\to\mathrm{O}}}{\mathrm{d}\Omega'} + \frac{\mathrm{d}\sigma_{\mathrm{X}\to\mathrm{X}}}{\mathrm{d}\Omega'}\,. \tag{3.4.28}$$

Integrating the equation (3.4.28) over Ω', we obtain:

$$\sigma_{\mathrm{X}}(\mathcal{E}) = \sigma_{\mathrm{T}}\int_{\Omega'=4\pi}\frac{3}{8\pi}\left(\frac{\mathcal{E}}{\mathcal{E}_{\mathrm{Cyc}}}\right)^2[\mu'^2\cos^2(\phi-\phi') + \sin^2(\phi-\phi')]\mathrm{d}\Omega'$$

$$\sigma_{\mathrm{X}}(\mathcal{E}) = \sigma_{\mathrm{T}}\frac{3}{8\pi}\left(\frac{\mathcal{E}}{\mathcal{E}_{\mathrm{Cyc}}}\right)^2\left[\int_0^1\int_0^{2\pi}\mu'^2\cos^2(\phi-\phi')\mathrm{d}\mu'\mathrm{d}\phi' + \int_0^1\int_0^{2\pi}\sin^2(\phi-\phi')\mathrm{d}\mu'\mathrm{d}\phi'\right]$$

that gives

$$\sigma_{\mathrm{X}}(\mathcal{E}) = \frac{\sigma_{\mathrm{T}}}{2}\left(\frac{\mathcal{E}}{\mathcal{E}_{\mathrm{Cyc}}}\right)^2\,. \tag{3.4.29}$$

We will use this equation for calculating the Rosseland mean opacity.

A little interlude Even though we restrict our discussion to the non relativistic case and to a frequencies domain well below the cyclotron frequency, we mention the fact that if we have let the energy $\mathcal{E}$ approach $\mathcal{E}_{\mathrm{Cycl}}$, the cross section would instead increase its value with respect to the Thomson cross section σ_{T}. Obviously a cross section value calculated by means of (3.4.29) might return physically unmeaningful results since we have developed that formula in a different approximation: though if one relaxes it and performs more rigorous

calculations for $\sigma \equiv \sigma(\mathcal{E})$, one would get a term $(\mathcal{E}-\mathcal{E}_{\rm Cycl})^{-2}$ that makes σ peak for $\mathcal{E} \to \mathcal{E}_{\rm Cycl}$. The values at which these maxima occur are called **resonances**.

In non-relativistic case the cross section has just one resonance for $\mathcal{E} = \mathcal{E}_{\rm Cycl}$ for the reason just pointed-out; in the full-relativistic case more than one resonances are expected, but calculations would be different and even more complicated to be described here.

3.4.4 The complete set of equations

Here we summarize all the equations and the corresponding boundary conditions adopted in this work. Recalling the hypotheses of local thermodynamic equilibrium and optically thick plasma,

$$P_{\rm rad}(x, H_x) = \frac{\epsilon_{\rm R}}{3}\,, \tag{3.4.30}$$

where the energy density $\epsilon_{\rm R}$ is expressed in terms of the flux assuming no incoming radiation at the boundary (non-illuminated atmosphere):

$$\epsilon_{\rm R} = \frac{2\mathcal{F}}{c}\,. \tag{3.4.31}$$

Hence equation (3.3.4) turns into:

$$P_{\rm rad}(x, h) = \frac{GM}{R^2}\left[7\rho_{\rm ff}(x)H_x \int_{h/R}^{H_x/R} \frac{{\rm d}t}{t(1+t)} + \frac{2}{3c}\mathcal{F}_{\rm Edd}(H_x)\right]\,, \tag{3.4.32}$$

where we introduce the further assumption that the flux is equal to the Eddington flux at the shock surface.

Evaluating the integral and substituting the expression for $\mathcal{F}_{\rm Edd} = GMc/k_\parallel R^2$ one obtains:

$$P_{\rm rad}(x, h) = \frac{GM}{R^2}\left\{7\rho_{\rm ff}(x)H_x\left[\lambda\left(\frac{H_x}{R}\right) - \lambda\left(\frac{h}{R}\right)\right] + \frac{2}{3k_\parallel}\frac{1}{(1+H_x/R)^2}\right\}\,, \tag{3.4.33}$$

where:

$$\lambda(x) \equiv \frac{1}{1+x} + \ln(x) - \ln(1+x) \tag{3.4.34}$$

results from the integration of the first addendum in the second term of equation (3.4.32).

For what concerns equation (3.3.9), if we substitute in it equations (3.4.16) in the same assumptions stated above, we obtain:

$$P_{\rm rad}(x,h) = \frac{2}{c}\mathcal{F}_{\perp,\rm esc}(h)\left[\frac{7}{d_h h}\int_x^{d_h/2}\rho_{\rm ff} z H_z k_\perp(z,h) z\,{\rm d}z + \frac{1}{3}\right]. \qquad (3.4.35)$$

3.5 Computational scheme

In order to determine the limiting luminosity produced by an accretion column, we will solve numerically the equations introduced in the previous Section. The main parameters of the model are:

- the **mass** M of the NS;
- the **radius** R of the NS;
- the value of the magnetic field at the NS surface B_0;
- the **mass-accretion rate** $\dot{M}$;
- the height at the center of the accretion column H_0.

M and R are fixed parameters and their values are reported in Tab. 3.5. B_0, $\dot{M}$ and H_0 can be changed. Once B_0 and $\dot{M}$ (or the total luminosity) are fixed, H_0 is varied iteratively until the numerical solution of the equation reaches convergence. The initial guess for H_0 is usually taken to be $0.75R$. First we introduce the correct dependencies of the parameter d_0, l_0 and $S_{\rm D}$, whose mathematical expressions depend on the height at which the disc interrupts[7]. We retrieve their values from the parameter l_0/d_0 and $l_0 d_0 \equiv S_{\rm D}$ reported in Mushtukov

[7]The disc can be divided in three zones according to the dominating pressure and opacity sources (Mushtukov et al. 2015b): the inner zone (the A-zone, dominated by radiation pressure), the intermediate zone (the B-zone, dominated by gas pressure and electron scattering) and the outer zone (the C-zone, dominated by Kramer opacity and gas pressure).

First-Guess Values	
M	$1.4\,\mathrm{M}_\odot$
R	$10^6\,\mathrm{cm}$
$\dot{M}$	$5\times10^{18}\,\mathrm{g\,s^{-1}}$
H_0	$0.75\times10^6\,\mathrm{cm}$

Table 3.1:

et al. (2015b). They are both functions of the magnetospheric radius R_M, with $R_\mathrm{M}\sim\mathcal{R}_\mathrm{A}\propto B^{4/7}$. For a disc interupted in the A-zone:

$$\frac{l_0}{d_0}\sim R_\mathrm{M}\propto B^{4/7} \tag{3.5.1}$$

$$S_\mathrm{D}\propto B^{-8/7} \tag{3.5.2}$$

(see equations 27-28, 30-31 in Mushtukov et al. (2015b)).

We calculate an initial guess for the temperature profile $T\equiv T(x,y)$ using equations (3.3.7, 3.4.2, 3.4.5, 3.4.16), that can be easily combined with simple algebra.

As can be seen temperature drops quickly towards the outer boundary of the accretion column.

1st step: opacity As already anticipated, we will use the non-relativistic approximation (3.4.29) for evaluating the electron scattering opacity for high magnetic-field strenghts. With such expressions we will calculate the Rosseland-mean opacity:

$$\frac{1}{\overline{k}_{\perp,B}}=\frac{\int_0^\infty k_{\perp,B}^{-1}(\mathcal{E})\partial\mathcal{B}(\mathcal{E},T)/\partial T\,\mathrm{d}\mathcal{E}}{\int_0^\infty\partial\mathcal{B}(\mathcal{E},T)/\partial T\,\mathrm{d}\mathcal{E}}\,, \tag{3.5.3}$$

where $\mathcal{B}(\mathcal{E},T)$ is the Planck distribution and $\mathcal{E}$ is photon energy:

$$\mathcal{B}(\mathcal{E},T)=\frac{2\mathcal{E}^3}{(hc)^2}\frac{1}{e^{\mathcal{E}/kT}-1} \tag{3.5.4}$$

and k is the opacity:

$$k=\frac{\sigma}{\mu_e m_\mathrm{P}}\,, \tag{3.5.5}$$

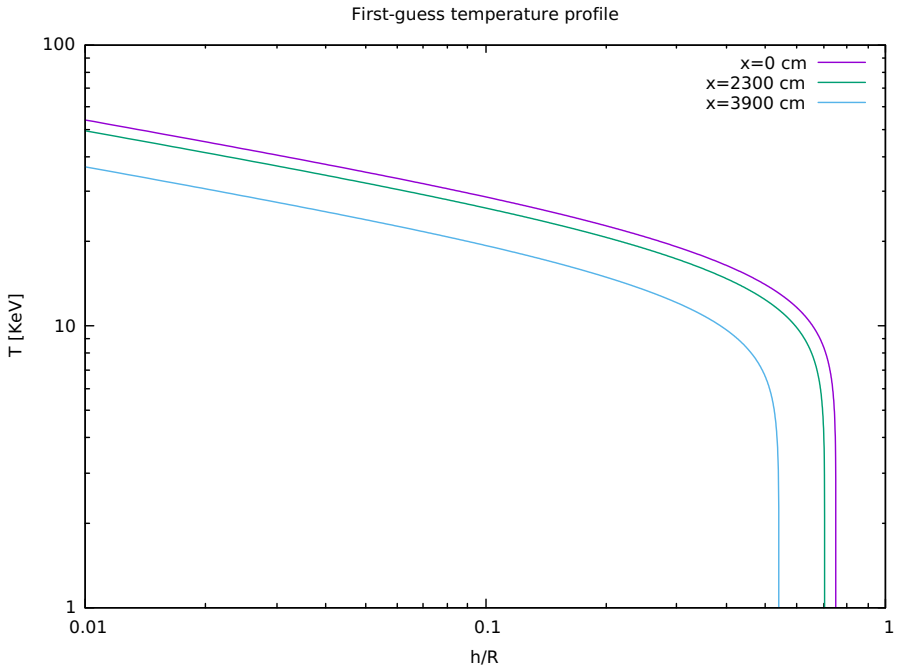

Figure 3.5: Initial temperature profiles for different values of x and for $\dot{M} = 5 \times 10^{18}\,\mathrm{g\,s^{-1}}$, $H_0 = 0.75R$ and $B_0 = 10^{12}\,\mathrm{G}$. Each one is computed at a fixed value of x indicated in the top-right of the diagram.

where μ_e is the mean molecular weight, m_P is the proton mass and σ is given by equation (3.4.29). Recall that, when we obtained it, we integrated on the incoming photon directions. Now we have to integrate it over the outcoming directions of the flux, that is:

$$\frac{1}{\overline{\sigma}_{\perp,B}} = \frac{2}{\sigma_\mathrm{T}} \left(\frac{\mathcal{E}_\mathrm{Cycl}}{kT} \right)^2 \frac{\int_{\Omega=4\pi} \int_0^\infty x^2 e^x (e^x - 1)^{-1} \,\mathrm{d}x \,\mathrm{d}\mu}{\int_0^\infty x^4 e^x (e^x - 1)^{-1} \,\mathrm{d}x}\,, \tag{3.5.6}$$

where we have substituted the analytic expression of $\partial\mathcal{B}/\partial T$ and $x = \mathcal{E}/kT$.

The integrals in (3.5.6) can be evaluated analytically because they can be reduced to particular cases of the *Bose-Einstein integrals* $\mathfrak{I}_\mathrm{BE}$ used in statistical

mechanics:

$$\mathfrak{I}_{\rm BE}(p) = \int_o^\infty \frac{x^{p-1}}{e^x - 1}\,{\rm d}x = \Gamma(p)\zeta(p) \quad \text{with}\, p > 1\,, \tag{3.5.7}$$

where $\Gamma(p)$ is the Euler's *Gamma* function and $\zeta(p)$ is the Riemann's *zeta* function.

Substituting these expressions, after a number of manipulations we finally obtain:

$$\overline{k}_{\perp,B} = \frac{2}{5}\pi^2 k_{\rm T} \left(\frac{kT}{\mathcal{E}_{\rm Cycl}}\right)^2 . \tag{3.5.8}$$

2nd step: base of the accretion column We need an estimate of the position of the base of the accretion column h_0. We restrict ourselves to the case $x = 0$ (center of the column). The value of h_0 is found imposing that the sum of the radiation and gas pressure is equal to the magnetic pressure, or:

$$P_{\rm rad}(0, h) + P_{\rm gas}(h) = P_{\rm mag}(h) \tag{3.5.9}$$

$P_{\rm mag}$ is given by equation (3.3.1), $P_{\rm rad}(0, h)$ by equations (3.4.33) and (3.5.9).

For typical values of the magnetic-field strenght h_0 is expected to be in the range between $[0.1, 100]$ cm: since $h_0 \ll H_0$, the final luminosity does not depend on this value as pointed out by Mushtukov et al. (2015b). Therefore we fixed it at $h_0 = 2.0$ cm.

3rd step: thickness of the sinking region We can see that in equation (3.3.9) the thickness of this region d_h appears as the upper boundary of an integral: we start with the quasi-parabolic-first guess profile of H_x reported in Sec. 3.4 and proceed iteratively follwing the treatment of Mushtukov et al. (2015b).

We start from equations (3.4.33) and (3.4.35) that are suitably combined together to give an integral recursive relation. We assume that $d_h(h_0) = d_0$ because h_0 is negligible compared to H_0.

We first evaluate $P_{\rm rad}(0, h_0)$ from equation (3.4.33). Then:

- we insert $P_{\rm rad}(0,h_0) \equiv P_{\rm rad}(0,h_0)|_{\rm II}$ in the l. h. s. of equation (3.4.35) and solve for $\mathcal{F}_{\perp,\rm esc}(h_0)$;
- $\mathcal{F}_{\perp,\rm esc}(h_0)$ can be inserted once more in equation (3.4.35) for retrieving an expression for $P_{\rm rad}(x,h_0) \equiv P_{\rm rad}(x,h_0)|_{\rm II}$;
- a second expression for $P_{\rm rad}(x,h_0) \equiv P_{\rm rad}(x,h_0)|_{\rm I}$ profile is obtained from (3.4.33).

The two equations are then combined together to get:

$$\int_x^{d_0/2} \rho_{\rm ff}(z) H_z k_\perp(z,h_0) z \, {\rm d}z = \left[\frac{P_{\rm rad}(0,h_0)|_{\rm II}}{P_{\rm rad}(x,h_0)|_{\rm I}} - \frac{1}{3} \right] \frac{d_0 h_0}{7} \, . \tag{3.5.10}$$

We search the value of H_x that solves this equation numerically for a given value of x.

d_h is then found inverting the piecewise linear interpolation of the table (x, H_x). $P_{\rm rad}(x,h)$ is finally calculated from equation (3.4.33).

4th step: luminosity Once d_h and $P_{\rm rad}$ have been computed, from equation (3.4.35) we can calculate $\mathcal{F}_{\perp,\rm esc}$.

As in equation (3.4.10), the total luminosity emitted by the accretion column is obtained integrating the radiative flux over the emitting surface (the walls of the accretion column):

$$\mathcal{L}'(H_0) = 4 l_0 \int_{h_0}^{H_0} \left(\frac{R+h}{R} \right)^{3/2} \mathcal{F}_{\perp,\rm esc}(h) \, {\rm d}h \, . \tag{3.5.11}$$

where the term $(1+h/R)^{3/2}$ in the integral accounts for the geometrical shape of the walls of the accretion column. As in Mushtukov et al. (2015b), the procedure is iterated: we take the radiation pressure $P_{\rm rad}(x,h)$ and via equation (3.3.7) a new temperature profile $T(x,h)$ is calculated. We then return to the 1st step and recalculate the opacities, radiation pressure, flux and finally the luminosity $\mathcal{L}'(H_0)$. The scheme is halted when the difference between two subsequent values of $\mathcal{L}'(H_0)$ is less than 0.01%.

If the calculations gives an accretion luminosity $\mathcal{L}'(H_0)$ that differs from what expected from the assumed mass-accretion rate:

$$\mathcal{L} = \frac{GM\dot{M}}{R} \tag{3.5.12}$$

the value of H_0 is udpated[8] and the whole calculation is repeated.

3.6 Results

The implementation of this model, as already said, was done by means of a numerical code written in `FORTRAN90`. We will refer to it as `MACHD` (`Maximum Accretion-Column Height calculator for a Dipolar magnetic field`) in the following (see Appendix A).

The accretion luminosity as a function of the height of the accretion column is shown in Fig. 3.9. As it can be seen, the curves for $B = 10^{14}$ G barely reach a luminosity $\mathcal{L} \gtrsim 10^{40}\,\mathrm{erg\,s^{-1}}$ comparable to M82X-2 (Bachetti et al. 2014) and predict no ULX pulsars with accretion luminosity greater than $\sim 3{\times}10^{40}\,\mathrm{erg\,s^{-1}}$.

In Fig. 3.6, 3.7, 3.8 we show the profiles of the physical quantities computed with our code coresponding to different values of the magnetic-field strenght and the accretion luminosity.

3.6.1 Physical quantities in the accretion column

We computed the following quantities:

- cross section $\sigma_0(h/R) \equiv \sigma(x = 0, h/R)$ (Fig. 3.6);
- effective temperature $T_{\rm eff}(h/R) = (\mathcal{F}_{\perp,\rm esc}/\sigma_{\rm SB})^{1/4}$, where $\sigma_{\rm SB}$ is the Stefan-Boltzmann constant (see Fig. 3.7);
- central temperature $T_0(h/R) \equiv T(x = 0, h/R)$ (Fig. 3.8).

[8] As the luminosity $\mathcal{L}(H_0)$ is expected to increase with H_0; if $\mathcal{L}' > \mathcal{L}$, the new tried value for H_0 must be lower and vice versa.

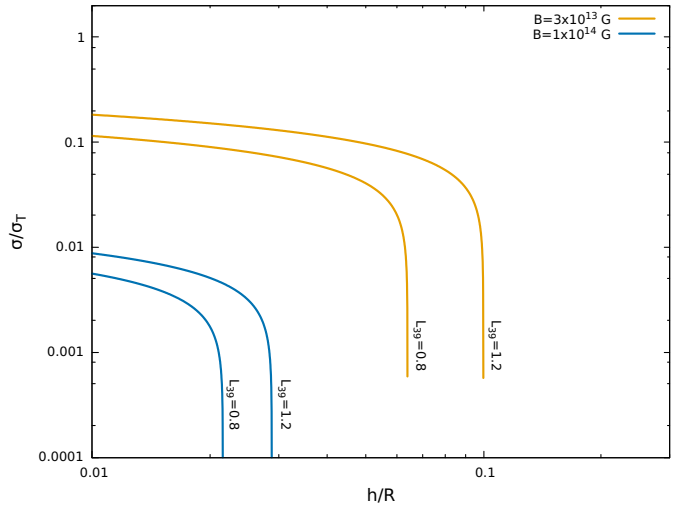

Figure 3.6: Cross section (in units of the Thomson-cross section $\sigma_{\rm T}$) for two different values of the magnetic-field strenght ($B = 3 \times 10^{13}$ G and $B = 10^{14}$ G). Each curve is labelled with the value of the luminosity in units of $10^{39}\,{\rm erg\,s^{-1}}$.

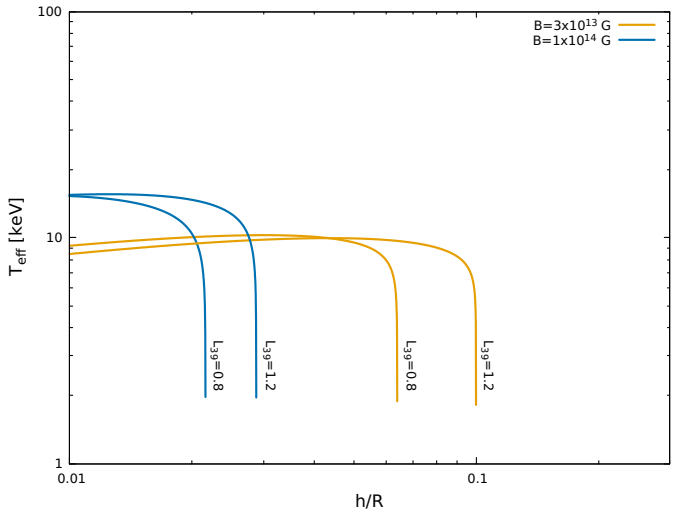

Figure 3.7: Effective temperatures (in keV) for two different values of the magnetic-field strenght ($B = 3 \times 10^{13}$ G and $B = 10^{14}$ G). Each curve is labelled with the value of the luminosity in units of $10^{39}\,{\rm erg\,s^{-1}}$.

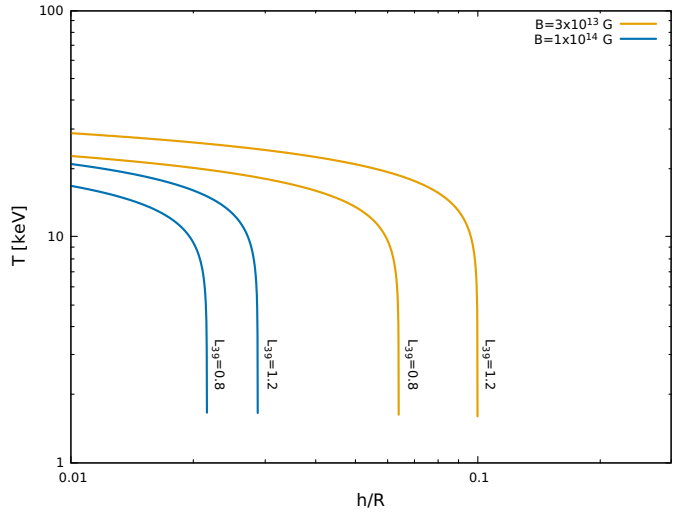

Figure 3.8: Temperatures (in keV) for two different values of the magnetic-field strenght ($B = 3 \times 10^{13}\,\mathrm{G}$ and $B = 10^{14}\,\mathrm{G}$). Each curve is labelled with the value of the luminosity in units of $10^{39}\,\mathrm{erg\,s^{-1}}$.

All the profiles show a sharp decline for $h \to H_0$ that univocally identifies the accretion-column luminosity for a fixed value of the magnetic-field strenght.

We particularly focus our attention on the values of the effective temperature in Fig. 3.7. Following a fixed-luminosity curve, it is possible to see that the value of T_{eff} increases with h/R reaching a maximum. This is not due to the temperature (that decreases), but to the geometrical thickness and the optical depth of the sinking region that obviously diminish for increasing h; in fact, from the definition of T_{eff}, in the hypothesis of local thermodynamic equilibium (3.3.7) and using the analytic estimate for the flux (3.4.3), it is:

$$T_{\mathrm{eff}} \simeq \left(\frac{3\sigma_{\mathrm{SB}}\tau_0}{a}\right)^{-1/4} T \sim \tau_0^{-1/4} T\,, \tag{3.6.1}$$

where τ_0 is the optical thickness along the direction perpendicular to the magnetic-field vector: thus, for small value of h, as h increases τ_0 decreases faster than T and T_{eff} raises. The opposite occurs for large enoigh value of h (close to h_0).

Looking at the figure, it is possible to understand also the influence of the magnetic field B. We demonstrated that $\overline{\sigma} \sim \mathcal{E}_{\rm Cycl}^{-2} \sim B^{-2}$. Thus, for a fixed luminosity the greater is the magnetic field, the lower is $\overline{\sigma}$. This affects the temperature: for high magnetic-field strenghts B less photons are retained in the accretion column, reducing the radiation pressure $P_{\rm rad}$ and hence the temperature.

This fact explains also why the accretion-column height H_0 is systematically lower for higher B as it can be seen from Fig. 3.6-3.8. The reduced radiation pressure does not allow to sustain anymore a pressure gradient capable to balance the weigth of high (i. e. *heavy*) accretion columns in hydrostatic equilibrium.

Finally if we compare the curves for different luminosities, it is possible to recognize that $\mathcal{L}$ increases with H_0. We know that the larger[9] the luminosity, the higher is the height of the accretion-shock over the NS-surface.

3.6.2 Accretion luminosity

The calculation of the luminosity of the accretion column is the main goal of our numerical calculations. As shown in Fig. 3.9 $\mathcal{L}$ is a monotonically increasing function of H_0 for a fixed magnetic field.

The curves computed with our `MACHD` numerical code do not perfectly match those of Mushtukov et al. (2015b), although they clearly show the same trend[10]. We discuss in this section some reasons that might account for this difference.

The choice of h_0 (the accretion-column base height) we have imposed should not affect the accretion-luminosity, as pointed out in Sec. 3.5 and by Mushtukov et al. (2015b); and no difference is indeed seen running the `MACHD` code with a different value of h_0.

[9] Larger at least than the critical luminosity $\mathcal{L}^*$ we introduced in Sec. 2.2.

[10] The fractional difference between them is $\lesssim 55\,\%$ for $B \lesssim 10^{14}\,\mathrm{G}$ and $\lesssim 80\,\%$ for $B \lesssim 10^{15}\,\mathrm{G}$, our curves typically providing higher values of $\mathcal{L}$.

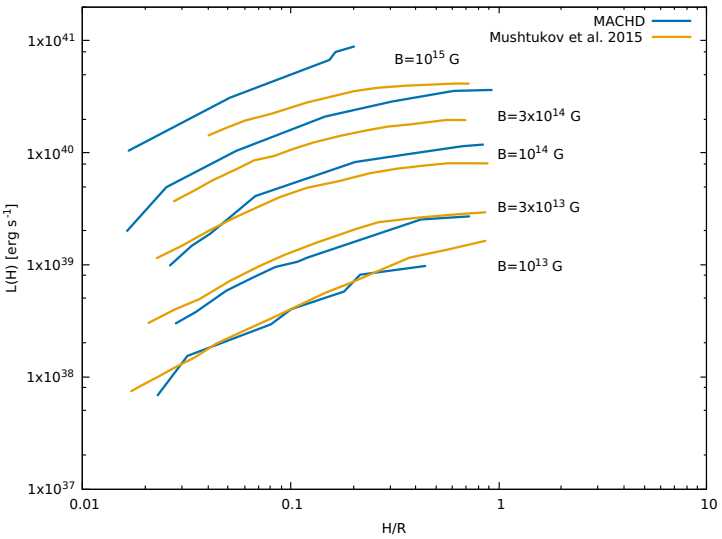

Figure 3.9: Accretion-column luminosities obtained with our `MACHD` code (*blue line*) compared to those reported by Mushtukov et al. (2015b) (*yellow line*). At fixed H/R the accretion luminosity $\mathcal{L}(H)$ increases with magnetic-field strenght as expected from the B-dependence of the cross section; the various curves refer to different values of $B = 10^{13}$ G, 3×10^{13}, 10^{14} G, 3×10^{14}, 10^{15} G.

On the other hand, we found that the expression of the cross section adopted in our model (3.5.8) gives value of σ systematically lower and luminosities systematically higher than those reported in Mushtukov et al. (2015b), especially for high accretion-column heights.

For a magnetic-field strenght $B = 10^{14}\,\mathrm{G}$ the cyclotron energy is $\sim 1\,\mathrm{MeV}$, and therefore we would expect:

$$\frac{\overline{k}_{\perp}}{k_{\mathrm{T}}} \sim 10^{-4} \tag{3.6.2}$$

for a temperature of the order of 10 keV (see eq. 3.5.8Fig. 3.8). However the value of $\sigma_{\perp}/\sigma_{\mathrm{T}}$ for the same temperature in Mushtukov et al. (2015b) is $\sim 10^{-2}$.

We found that if multiplying by a factor 20 the cross section (3.5.8) our results turn out to be in fair agreement with those of Mushtukov et al. (2015b). Thus we have adopted the following expression for the:

$$\overline{k}_{\perp,B} = 8\pi^2 k_{\mathrm{T}} \left(\frac{kT}{\mathcal{E}_{\mathrm{Cycl}}}\right)^2 . \tag{3.6.3}$$

The results shown in this Chapter have been obtained under this assumption. Despite an extensive search we could not find the reason for the different coefficient of the cross section. At the time of writing we are still investigating the origin of the problem, checking all the various constants and inputs in the code. However, it is reassuring that, after rescaling it, the overall dependence of the physical quantities in the accretion column is fairly well reproduced.

We note that the model of Mushtukov et al. (2015b) provides results that are accurate within a factor of ~ 2 : one of the source of uncertainty is in the assumption on the exponent ξ of the power law (3.4.14) that describes the spatial dependence of the velocity (and thus the density). Tests run by Mushtukov et al. show that changes in ξ do not affect significantly the value of $\mathcal{L}$ that may vary by a factor ~ 2. The same level of uncertainty applies also to our model[11].

[11] We roughly estimated that $\langle \mathcal{L}_{\texttt{MACHD}} \rangle \sim 1.85 \langle \mathcal{L}_{\mathrm{Mushtukov}} \rangle$ for $B = 10^{15} G$, for which the difference is the largest.

Since we are interested in understanding the existence of brighter ULX Pulsars, in the next chapter we will modify the magnetic field topology adding a multipolar component to the pre-existing dipolar component.

Chapter 4

Including multipolar components in the magnetic field

The extreme properties of NGC 5907 ULX-1 cannot be explained even invoking the model of Mushtukov et al. (2015b) introduced in the previous Chapter. A possible solution to this problem is presented in this Chapter, in which a higher order in the multipolar expansion of the magnetic field is considered. Sec. 4.1-4.2 describe the implementation of this new model, which returns the accretion luminosity of a magnetized NS for the aforementioned magnetic field topology and is carried out in a new numerical (`FORTRAN90`) code (`MACHM`); Sec. 4.3 presents the results of the computations performed with this code.

4.1 Introduction

The model of Mushtukov et al. (2015b) introduced in the previous chapter gives a maximum accretion luminosity of roughly $1 \div 3 \times 10^{40}\,\mathrm{erg\,s^{-1}}$ for a

magnetar-like magnetic-field strenght ($B \sim 10^{15}$ G). This luminosity is adequate to account for the ULX Pulsar observed by Bachetti et al. (2014).

However the more recent discovery within the EXTraS project of an ULX in NGC 5907 with an unexpectedly high (isotropic) luminosity $\gtrsim 10^{41}\,\mathrm{erg\,s^{-1}}$ would require a magnetic-field strenght $\gtrsim 10^{15}$ G according to the scenario discussed in Sec. 2.3.1. This is so high that the propeller effect would inhibit matter from accreting onto NS surface because of the high centrifugal forces.

However as already suggested in Israel et al. (2017a,b), the model of Mushtukov et al. (2015b) might be retained assuming that the NS-magnetic field has multipolar components.

4.2 Multipolar field

The great majority of theoretical models concerning the physics of the NSs typically assume a dipolar geometry for the magnetic field of the star. But in the last decade the need to consider more complex magnetic field configurations has emerged: evidence for this comes, e.g., from the modelling of thermal emission from the so-called X-ray dim isolated neutrons stars, the high pulsed fraction of which can not be reconciled with a dipole field (Zane & Turolla 2006), and from the detection of a phase-variable absorption feature in the magnetar SGR 0418+ 5729 (Tiengo et al. 2013).

Similarly multipolar magnetic fields (which fall off more steeply with the radial distance) might account for the still unexplained luminosity of NGC 5907 ULX. In order to verify this hypothesis, we start assuming that the magnetic field has a multipolar component. We then write the magnetic field at distance[1]

[1]We will replace r with $R + h$ in the accretion column, hence:

$$B_{\mathrm{tot}}(r) = \sum_{l=1}^{N} B_l \left(\frac{R}{R+h}\right)^{l+2}$$

.

r by means of the following multipolar expansion:

$$B_{\rm tot}(r) = \sum_{l=1}^{N} B_l \left(\frac{R}{r}\right)^{l+2} , \tag{4.2.1}$$

(Arons 1993) where the coefficients B_l are the values of the magnetic field at $r = R$, and where for the sake of simplicity we have neglected the non-trivial angular dipendence (see e. g. Page & Sarmiento 1996). It is easy to verify that the $l = 1$ component corresponds to a dipolar magnetic field. Hence we will call in the following:

$$B_{\rm dip} = B_1 \left(\frac{R}{r}\right)^3 \tag{4.2.2}$$

$$B_{\rm multi} = B_2 \left(\frac{R}{r}\right)^4 . \tag{4.2.3}$$

Halting the expansion (4.2.1) to the second order it results $B_{\rm tot} = B_{\rm dip} + B_{\rm multi}$. In the following we will assume that near the accretion column a multipolar term becomes important. Given that the dipole component survives at $r \gg R$, the field close to the Alfvén radius is dominated by $B_{\rm dip}$ and this ensures that accretion can take place (low values of the dipolar field $B_1 \lesssim 2 \times 10^{13}$ G). At the same time, a large accretion column luminosities can be produced (high values of the multipolar field $B_2 \sim 10^{14} \div 10^{15}$ G).

4.2.1 Numerical implementation

In order to compute the accretion luminosity for a new magnetic-field geometry, we wrote a new code in `FORTRAN90` that preserves the general structure of `MACHD` but incorporates an additional multipolar component for the magnetic field. We called the new code `MACHM` (`Maximum Accretion-Column Height calculator for a Multipolar magnetic field`).

In the new code we modified the cross section $\sigma_\perp$, that accounts for interactions whithin the accretion column of photon moving perpendicular to the magnetic-field direction. For small distances from the NS, the steeper behaviour

of the multipolar component dominates over the dipolar one: then we take equation (3.6.3) and insert in it the multipolar term that yields:

$$\overline{k}_{\perp} \sim B_2^{-2}\,. \tag{4.2.4}$$

But as the distance from the NS increases, the multipolar term becomes negligible with respect to the dipolar one: we leave then unchanged the expressions for the values of l_0/d_0 and $S_{\rm D}$ that are functions of the magnetospheric radius $R_{\rm M}$ where the dipolar component dominates. Equations (3.5.1,3.5.2) then hold unchanged with $B = B_1$.

For a fixed accretion-column height we obtain from equations (3.4.10, 3.5.1, 3.5.2, 4.2.4):

$$\mathcal{L} \sim B_1^{4/7} B_2^2\,. \tag{4.2.5}$$

We expect then that increasing B_2 will enhance the luminosity far more than increasing B_1.

4.3 Results

The inclusion of a multipolar component in the magnetic-field topology gives results that are in agreement with our expectations. We show in Fig. 4.1 a comparison between two profiles of accretion luminosity for a dipolar component of 10^{14} G and a multipolar component of the magnetic field. The latter may in principle account for the huge luminosity of NGC 5907 ULX.

In Fig. 4.1 the two profiles are calculated with the same value of the magnetic field for the dipolar component B_1; changing B_1, luminosity would not vary significantly for the reasons we discussed in the previous section.

In Figures 4.2-4.4 we show the physical quantities (temperature, effective temperature and cross section) of the accretion column computed with `MACHM` and compare them with these results obtained with `MACHD` for the same value of the luminosity. In order to do that, we fix:

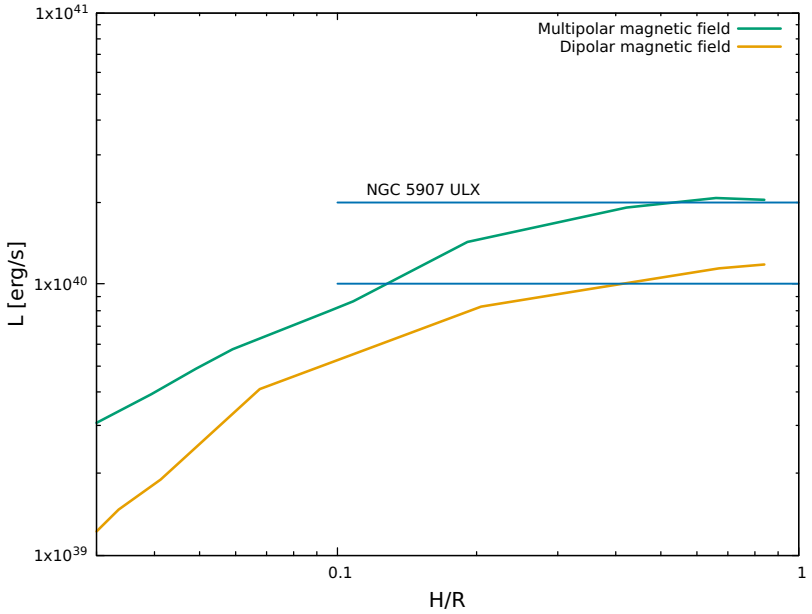

Figure 4.1: Accretion luminosity for two different magnetic-field topologies. As labelled, the green solid line represents the luminosity of an ULX Pulsar with a multipolar component $B_2 = 2 \times 10^{14}\,\mathrm{G}$; the yellow solid line represents the luminosity of an ULX Pulsar obtained with `MACHD`, with a dipolar field $B_1 = 3 \times 10^{13}\,\mathrm{G}$. The thick blue lines represent the luminosity range to which NGC 5907 ULX must belong; we have also used a beaming factor $b = 1/7$ (Israel et al. 2017b).

- the luminosity $\mathcal{L}$;

- the dipolar component of the magnetic field B_1.

The value of B_1 was choosen in order to let both codes (`MACHD` and `MACHM`) converge to the same value of the luminosity (when $B_2 = B_1$). We calculated the maximum accretion-column height H_0 with a fixed luminosity $\mathcal{L} = 10^{40}\,\mathrm{erg\,s^{-1}}$ for $B_1 = 10^{14}\,\mathrm{G}$.

The behaviour of the physical quantities in the accretion-colum is similar to that for the dipolar case, but we discuss them once more because it is worth to distinguish the contributions of the dipolar and the multipolar components of the NS-magnetic field.

The cross section σ depends only on the multipolar component of $\mathbf{B}$ for the reason we already pointed out. Since we assumed $B_2 = 1.2 \times 10^{15}\,\mathrm{G}$, the cross section for the multipolar component is significantly lower (see Fig. 4.4). If one had used $B_2 = 10^{14}\,\mathrm{G}$ no significant differences would have been present. The multipolar geometry, that reflects upon the different power index $l + 2 = 4$ appearing in equation (4.2.1) influences rather the slope of the curves.

Similar considerations can also be made for the behaviour of the temperature $T_0(h/R)$ and the effective temperature $T_{\mathrm{eff}}(h/R)$. As before the temperature shows a weaker dependence on the magnetic field than the effective temperature, since $T_0 \sim [\mathcal{F}_{\perp,\mathrm{esc}} \int \rho_{\mathrm{ff}} H_z k_\perp(z,h) z\,\mathrm{d}z]^{1/4}$; as $\mathcal{F}_{\perp,\mathrm{esc}} \sim k_\perp^{-1}$, we understand that there should not be a strong dependence on the opacity $k_\perp$. We recall that a lower value of σ let the photons escape more easily, thus cooling the accretion column.

Also the effective temperature T_{eff} is subject to changes similar to those noticed for a high dipolar magnetic field, whose luminosity profile has been calculated by `MACHD`. In the multipolar case, equations 3.4.35, 3.5.1, 3.5.2, 4.2.4 show that

$$T_{\mathrm{eff}} \sim B_1^{1/14} B_2^{1/2}\,. \tag{4.3.1}$$

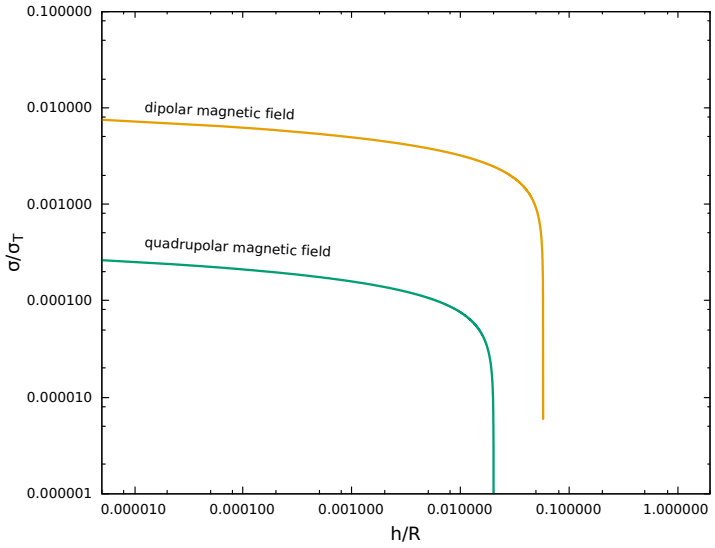

Figure 4.2: Electron scattering cross section as function of h/R for a multipolar magnetic field (`MACHM`, *green line*, computed for $B_2 = 1.2 \times 10^{15}\,\mathrm{G}$) compared with that for a dipolar magnetic field (`MACHD`, *yellow line*). In both cases, $B_1 = 10^{14}\,\mathrm{G}$ and $\mathcal{L} = 10^{40}\,\mathrm{erg\,s^{-1}}$.

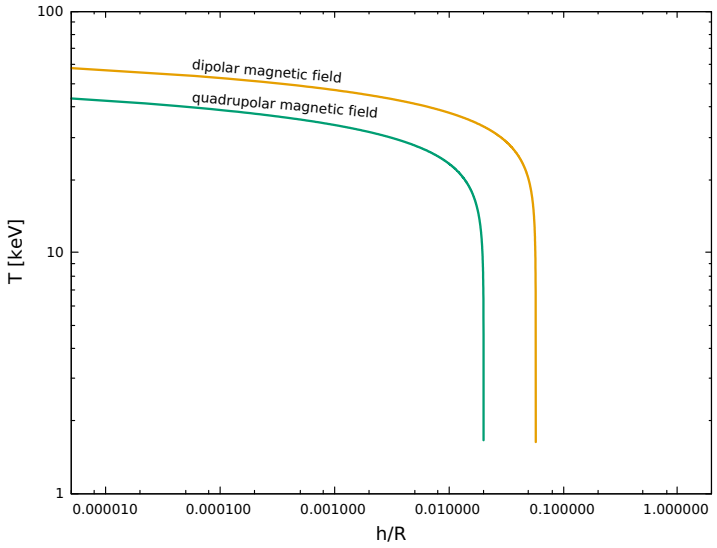

Figure 4.3: Temperature as function of h/R for a multipolar magnetic field (`MACHM`, *green line*, computed for $B_2 = 1.2 \times 10^{15}\,\mathrm{G}$) compared with that for a dipolar magnetic field (`MACHD`, *yellow line*). In both cases, $B_1 = 10^{14}\,\mathrm{G}$ and $\mathcal{L} = 10^{40}\,\mathrm{erg\,s^{-1}}$.

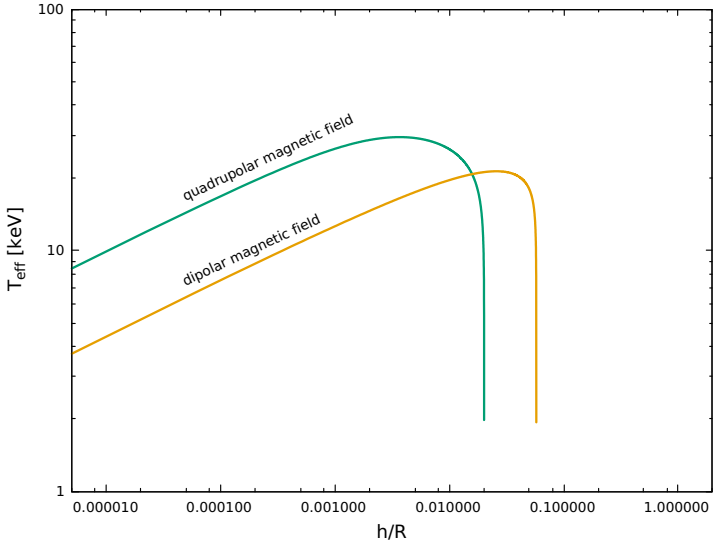

Figure 4.4: Effective temperature as function of h/R for a multipolar magnetic field (`MACHM`, *green line*, computed for $B_2 = 1.2 \times 10^{15}\,\mathrm{G}$) compared with that for a dipolar magnetic field (`MACHD`, *yellow line*). In both cases, $B_1 = 10^{14}\,\mathrm{G}$ and $\mathcal{L} = 10^{40}\,\mathrm{erg\,s^{-1}}$.

Once more we realize that the dipolar magnetic field is less important than the multipolar one. As discussed in Sec. 3.6 we see that the higher is the magnetic-field strenght, the smaller is the accretion-column height where $T_{\rm eff}$ goes to zero. High magnetic-field strenghts imply lower σ, so more radiation will be released and the lower radiation pressure will not be able to sustain a heavy and extended accretion-column.

Conclusions

Ultraluminous X-ray Sources (ULXs) are non-nuclear, point-like sources in external galaxies compact objects whose luminosity largely exceeds the Eddington limit for a $10\,M_{\odot}$ compact object. Until few years ago ULXs have always been modelled as accreting BHs, but the discovery of a pulsing ULX in the nuclear region of the galaxy M82 (M82 X-2, Bachetti et al. 2014) and of two other pulsars thereafter (NGC 7793 P13, Israel et al. 2017a, Fürst et al. 2016; NGC 5907 X-1, Israel et al. 2017b) changed completely our view of ULX and forced us to consider accretion-powered pulsars as alternative model. NGC 5907 ULX-1 (Israel et al. 2017b), in particular, challenges the model of accretion onto magnetized NSs (Mushtukov et al. 2015b). As suggested by (Israel et al. 2017b), a more complex magnetic field topology may be required to account for the observational properties of this source.

After having implemented the model of Mushtukov et al. (2015b) in Chap. 3 with the code `MACHD` (written in `FORTRAN90`), we performed a new calculation of the luminosity emitted by a magnetized NS including a multipolar component in the radial dependence of the magnetic field. The results of the new computations are discussed in Chap. 4 represent the main result of this Thesis. We found that the inclusion of a multipolar component may in principle account for the very high luminosity of NGC 5907 ULX-1, in agreement with the suggestion made by Israel et al. (2017b).

Future dedicated X-ray timing observations will allow us to constrain the orbital period of NGC 5907 ULX-1 and to determine the contribution of the orbital motion to the variation of the spin period: this will indeed permit to perform a more accurate modelling of this source.

Appendices

Appendix A

Surveying the X-ray Universe

The available data about ULXs were collected in last decades with X-ray space telescopes, whose aim and properties are summarized in this Appendix.

A.0.1 XMM-Netwon

The *High Throughput X-ray Spectroscopy Multi-Mirror Mission* (XMM) *Newton* was launched in 1999 by ESA and covers the $0.1 \div 10\,\mathrm{keV}$ energy band. It is equipped with three X-ray telescopes each of them with 58 gold coated mirrors, whose grazing incidence angles are between 17 and 42 arcmin (Jansen et al. 2001); on the focal plane there are two reflection grating spectrometers and three imaging instrument, the *European Photon Imaging Camera* (EPIC), composed of three different cameras (EPIC-pn, EPIC-MOS1, EPIC-MOS2).

A significant fraction of the available observation of ULXs has been collected by XMM Newton EPIC camera. Recently the EPIC-pn data were re-analyzed looking for both periodic and aperiodic variability within the framework of the EXTraS (*Exploring the X-ray Transient and variable Sky*) project.

A.0.2 Chandra X-ray Observatory

The Chandra X-ray Observatory is a NASA mission launched on 23rd July 1999 that aims at observing high-energy astrophysics phenomena involving BHs and NSs. The Chandra X-ray telescope, also known as *Advanced X-ray Astrophysics Facility* (AXAF), is equipped with two focal plane cameras, the High Resolution Camera and the Advanced CCD Imaging Spectrometer (Weisskopf 2012). The main strenght of the AXAF telescope lies in the mirrors forming the *High Resolution Mirror Assembly* (HRMA): mirrors are indeed polished with a great precision and are coated to ensure a large reflectivity for the incident X-rays. The angular resolution of the HRMA is about 0.2 arcsec.

A.0.3 NuSTAR

The *Nuclear Spectroscopic Telescope Array* is a X-ray mission launched by NASA in June 2012 with two co-aligned telescopes built with a multilayer-coated Wolter-I conical approximation X-ray optics. The alignment between the mirror module and the instrument module is constantly monitorated by means of two laser-metrology units (see Fig. A.1). Each of the two telescopes has 133 concentric, confocal shells made by slumping glass. On their focal plane there are two Cadmium Zinc Telluride Detectors operating in the $[3 - 79\,\mathrm{keV}]$ energy band. The unprecedent (at these energies) angular resolution of NuSTAR is ~ 12", and its field of view is $\sim 10'$.

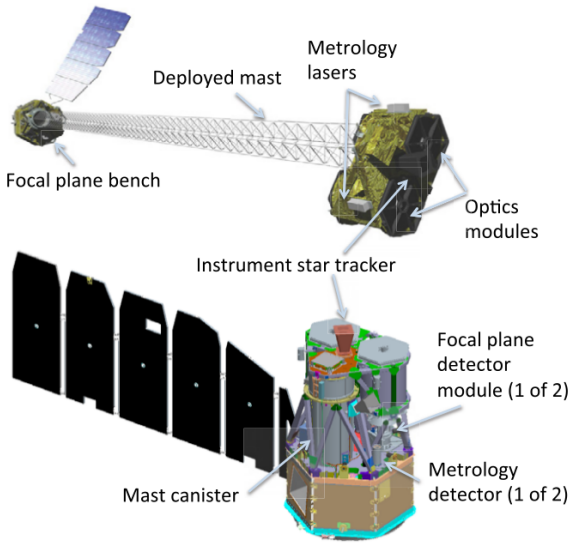

Figure A.1: The NuSTAR observatory setup Harrison et al. (2013).

Appendix B

The MACHM numerical code

```
!*******************************************************************************
!*     Maximum Column Height calculator for a Multipolar magnetic field (MACHM)  *
!*                                                                               *
!* This program associates the height of an accretion column that raise above the *
!* surface of an accreting Neutron Star (NS) in hydrostatic equilibrium for an    *
!* input luminosity.                                                             *
!* M is the mass of the NS, R is the radius of the NS, mdot is the mass-accretion *
!* rate, dB is the dipolar magnetic-field strenght, qB is the multipolar          *
!* magnetic-field strenght                                                       *
!* UNITS ARE IN CGS                                                              *
!*                                                                               *
!*******************************************************************************
PROGRAM machq
  IMPLICIT none
  INTEGER, PARAMETER :: xnum=1000, hnum=1000
  REAL(kind=8) :: integrate,lambda,gfunc,prad,zero
  REAL(kind=8) :: mdot,z_temperature,base_calc,pgas,pmag
  REAL(kind=8), PARAMETER :: R=1d6,M=2.786d33
  REAL(kind=8), PARAMETER :: G=6.67259d-8,c=2.99792458d10,a=7.5646d-15
  REAL(kind=8), PARAMETER :: mue=1.17,mh=1.6726219d-24
  REAL(kind=8), PARAMETER :: st=6.6524d-25, kt=0.3399371
  REAL(kind=8), PARAMETER :: pi=3.1415926
  REAL(kind=8), DIMENSION(xnum) :: x
  REAL(kind=8), DIMENSION(hnum) :: y
  REAL(kind=8), DIMENSION(hnum) :: fesc
  REAL(kind=8), DIMENSION(xnum,hnum) :: temp,vechx
  REAL(kind=8), DIMENSION(xnum,hnum) :: integrandum,radprxh,opxh
  REAL(kind=8), DIMENSION(xnum) :: z_integrandum,baseop
  REAL(kind=8) :: dx,dy,dyh
  REAL(kind=8) :: rhoff,sd,d0,l0
  REAL(kind=8):: H0,hb
  REAL(kind=8) :: dB,qB
  REAL(kind=8) :: oint,prado,f_esc0,height
  REAL(kind=8), DIMENSION(xnum) :: ho_int,radpr,nHx,opint,lint,Hx
  REAL(kind=8), DIMENSION(hnum) :: nh,dh
  REAL(kind=8) :: lum,lump,flum,slum,diff
  REAL(kind=8) :: tol,luminosity,difflump,difflum,lam
  REAL(kind=8) :: ratio,aratio,bratio,asd,bsd,ar,br,xop,quadrupole,basemag
```

```
  REAL(kind=8), DIMENSION(hnum) :: dmag
  INTEGER :: k,j,nptint,iter
  dB=3.0d1
  qB=1.2d15
  lum=1.0d40
  mdot=lum*R/(G*M)
  H0=0.03d0*R
  tol=5.0d-2
  lump=lum
  lam=0.5d0
  hb=2.0d0
  WRITE(*,'(A,E12.6,A,F9.6,A,I2,A)') 'Luminosity is ', lum, ' erg/s'
  WRITE(*,'(A)') '--------------------------------------------------'
  WRITE(*,*) ''
  difflum=2.0d0*tol
  WRITE(*,'(1X,A,6X,A,11X,A)') 'k','Max height(k)', 'Luminosity(k)'
  WRITE(*,'(A)') '--------------------------------------------------'

  !--->FIRST WHILE LOOP STARTS HERE

  DO WHILE(difflum>tol)
  iter=iter+1

  aratio=44.0d0*lam*( (M/1.989d33)**(8.0d0/7.0d0) )*&
  ( (R*1.0d-6)**(3.0d0/7.0d0) )*( (dB*1.0d-12)**(4.0d0/7.0d0) )*&
  ( (1.0d-39*lum)**(-9.0d0/7.0d0) )

  asd=1.3d10*( lam**(-2.0d0) )*( (1.0d-39*lum)**(11.0d0/7.0d0) )*&
  ( (dB*1.0d-12)**(-8.0d0/7.0d0) )*( (M/1.989d33)**(-9.0d0/7.0d0) )*&
  ( (R*1.0d-6)**(8.0d0/7.0d0) )

  bratio=80.0d0*( lam**(-1.0d0/20.0d0) )*( (M/1.989d33)**(19.0d0/35.0d0) )*&
  ( (dB*1.0d-12)**(-1.0d0/35.0d0) )*( (1.0d-39*lum)**(-13.0d0/70.0d0) )

  bsd=7.0d9*( lam**(-19.0d0/20.0d0) )*( (1.0d-39*lum)**(19.0d0/70.0d0) )*&
  ( (dB*1.0d-12)**(-41.0d0/70.0d0) )*( (M/1.989d33)**(-24.0d0/35.0d0) )*&
  ( (R*1.0d-6)**(129.0d0/70.0d0) )
  IF (1.0d-39*lum<0.2d0*(dB*1.0d-12)**(6.0d0/11.0d0) ) THEN
     ratio=bratio
     sd=bsd
     WRITE(*,*) 'Disc interrupted in B-zone'
  ELSE
     ratio=aratio
     sd=asd
     WRITE(*,*) 'Disc interrupted in A-zone'
  END IF
  d0=sqrt(sd/ratio)
  l0=sqrt(sd*ratio)
  WRITE(*,'(1X,A,7X,A,7X,A,1X)') 'd0','sd','l0'
  WRITE(*,'(E9.3,1X,E9.3,1X,E9.3)') d0,sd,l0

! Parameters

  nptint=1000
  dx=(log10(0.5d0*d0)-1d-8)/(xnum-1)
  dy=(1.0d0-hb/H0)/(hnum-1)
  dyh=1.0d2/(hnum-1)
  DO k=1,xnum
  !independent variable across the accretion column (x)
     x(k)=1.0d-8+(k-1)*dx
     x(k)=10.0d0**x(k)
  END DO
```

```
x(xnum)=0.5d0*d0
DO k=1,xnum
  IF (2.0d0*x(k)/d0>1.OR.2.0d0*x(k)/d0<0) THEN
     WRITE(*,*) 'eta(',k,')= ',2.0d0*x(k)/d0
  END IF
END DO
OPEN(unit=1,file='test.dat', action='write')
DO k=1,xnum
   Hx(k)=hb+height(x(k),H0-hb,R,d0)
   IF (Hx(k)<0) THEN
     DO j=1,xnum
        WRITE(1,*) (2.0d0*x(j)/d0)**2.0d0,Hx(j)
     END DO
   END IF
END DO
CLOSE(1)
DO j=1,hnum
!(in)dependent variable along the accretion column (h/Hx)
   y(j)= hb/H0 + (j-1)*dy
END DO

y(hnum)=1.0d0

!---------------------------------------------------------------------
!
! Step (i) iteration procedure
!
DO k=1,xnum
   DO j=1,hnum
      temp(k,j)=z_temperature(x(k),y(j),Hx(k),mdot,M,R,d0,sd)
      IF (temp(k,j)/=temp(k,j)) THEN
         WRITE(*,*) k,2.0d0*x(k)/d0,temp(k,j),y(j),Hx(k)
      END IF
   END DO
END DO
WRITE(*,'(I2,2X,E22.12,2X,E22.12)') iter,H0,slum
flum=lum
slum=2.0d0*lum
diff=2.0d0*tol
difflum=2.0d0*tol
!
!--->SECOND WHILE LOOP STARTS HERE
!
DO WHILE (diff>tol)
flum=slum
!radiation pressure for x=0 and h=hb ----> Eq. (16)
prado=prad(Hx(1),hb,M,R,mdot,sd)
basemag=quadrupole(qB,hb,R)
DO k=1,xnum
  baseop(k)=xop(basemag,temp(k,1))
END DO
DO k=1,xnum
   z_integrandum(k)=Hx(k)*baseop(k)*rhoff(M,R,mdot,sd,Hx(k))*x(k)
END DO
oint=integrate(xnum,z_integrandum,0d0,0.5d0*d0)                  !eq. (17)
f_esc0=0.5d0*c*prado*( (7.0d0/(d0*hb))*oint+1.0d0/3.0d0)**(-1)   !flux in eq. (17)
DO k=1,xnum
   ho_int(k)=integrate(nptint,z_integrandum,x(k),0.5d0*d0)
   radpr(k)=( 2.0d0*f_esc0/c )*( (7.0d0/(hb*d0))*ho_int(k) +&
   1.0d0/3.0d0 )!from eq. (17)
END DO
```

```
DO k=1,xnum
  DO j=1,hnum
    vechx(k,j)=gfunc(y(j)*Hx(1),sd,hb,M,R,mdot,radpr(k))
   END DO
END DO
nHx(1)=Hx(1)
DO k=2,xnum
  !the array nHx(k) returns a sampling for the new H(x) profile
  nHx(k)=zero(hb,Hx(1),xnum,vechx(k,:))
END DO
nHx(xnum)=hb

!linear fit of vector x(Hx) to get xout(h)=d(h)
CALL inverse(xnum,hnum,nHx(xnum),nHx(1),x,nHx,nh,dh)

nh=nh/nHx(1)
!
! Step (v) iteration procedure
!
DO k=1,xnum
   DO j=1,hnum
      radprxh(k,j)=prad(nHx(k),nh(j)*nHx(k),M,R,mdot,sd)  !from eq. (16)
   END DO
END DO
DO j=1,hnum
   dmag(j)=quadrupole(qB,y(j)*Hx(1),R)
END DO
DO k=1,xnum
   DO j=1,hnum
      opxh(k,j)=xop(dmag(j),temp(k,j))
   END DO
END DO
DO k=1,xnum
   DO j=1,hnum
   integrandum(k,j)=nHx(k)*opxh(k,j)*rhoff(M,R,mdot,sd,nHx(k))*x(k)
   END DO
END DO
DO j=1,hnum
   opint(j)=integrate(hnum,integrandum(:,j),0d0,0.5d0*dh(j))
   fesc(j)=0.5d0*c*radprxh(1,j)*( (7d0/(nh(j)*nHx(1)*dh(j)))*&
   opint(j)+(1d0/3d0) )**(-1) !from eq. (17)
END DO
!
! Step (vi) iteration procedure
!
DO j=1,hnum
   lint(j)=( ((R + nh(j)*nHx(1))/R)**1.5d0 )*fesc(j)
END DO
luminosity=4d0*l0*integrate(hnum,lint,0.0d0,Hx(1))
slum=luminosity
mdot=slum*R/(G*M)
diff=abs(flum-slum)/flum

asd=1.3d10*( lam**(-2.0d0) )*( (1.0d-39*slum)**(11.0d0/7.0d0) )*&
( (dB*1.0d-12)**(-8.0d0/7.0d0) )*( (M/1.989d33)**(-9.0d0/7.0d0) )*&
( (R*1.0d-6)**(8.0d0/7.0d0) )
bsd=7.0d9*( lam**(-19.0d0/20.0d0) )*( (1.0d-39*slum)**(19.0d0/70.0d0) )*&
( (dB*1.0d-12)**(-41.0d0/70.0d0) )*( (M/1.989d33)**(-24.0d0/35.0d0) )*&
( (R*1.0d-6)**(129.0d0/70.0d0) )

IF (1.0d-39*slum<0.2d0*(dB*1.0d-12)**(6.0d0/11.0d0) ) THEN
   sd=bsd
```

```
  ELSE
     sd=asd
  END IF
  !
  ! Step (vii) iteration procedure
  !
  Hx=nHx
  DO k=1,xnum
     DO j=1,hnum
        temp(k,j)=( (3d0/a)*prad(Hx(k),y(j)*Hx(k),M,R,mdot,sd) )**0.25d0
        IF ( temp(k,j)/=temp(k,j) ) THEN
           WRITE(*,*) 'Temperature returns Nan! The input of prad was',Hx(k)
        END IF
     END DO
  END DO
  END DO

  !--->SECOND WHILE LOOP ENDS HERE

  difflump=abs(slum-lump)/lum
  difflum=abs(slum-lum)/lum
  IF ((slum-lum) > 0) THEN
     IF ((difflump/difflum) < 0.05 .AND. difflum > 0.2) THEN
      H0=0.9*H0
     ELSE
       H0=(1.0-1.0/min(5.0*iter,1.0d6))*H0
     END IF
  ELSE
     IF ((difflump/difflum) < 0.05 .AND. difflum > 0.2) THEN
       H0=1.1*H0
     ELSE
       H0=(1.0+1.0/min(5.0*iter,1.0d6))*H0
     END IF
  END IF
  lump=slum
  END DO

  !--->FIRST WHILE LOOP ENDS HERE
  !
  !
  WRITE(*,*) ':::::::::::::::::::::::::::::::::::::::::::::::::::::::::::::'
  WRITE(*,*) ':::::::::::::::::MAXIMUM ACCRETION LUMINOSITY OF AN ULX::::::::'
  WRITE(*,*) ':::::::::::::::::::::::::::::::::::::::::::::::::::::::::::::'
  WRITE(*,*) ''
  WRITE(*,*) 'Mns (Msun)  Rns (km)  Mdot (g/s)  dB0 (Gauss)  L (erg/s)     &
  tolerance  ','Height (Rns)  Linp (erg/s)  d0 (cm)       l0 (cm)       S0 (cm2)'
  WRITE(*,'(F7.3,A,F7.3,A,E9.3,A,E9.3,A,E12.6,A,F9.6,A,F8.5,A,E12.6,A,E12.6 &
,A,E12.6,A,E12.6)')&
              M/1.989d33,'     ',R/1d5,'    ',mdot,'   ',dB,'   ',slum,' ',difflum,'  ',&
              H0/R,'       ',lum,'  ',d0,'  ',l0,'  ',sd
END PROGRAM machq
!
!================================================================================
!                               FUNCTIONS AND SUBROUTINES
!
!This function computes magnetic pressure
REAL(kind=8) FUNCTION pmag(h,R,magp)
  IMPLICIT none
  REAL(kind=8) :: h,magp,R
  REAL(kind=8), PARAMETER :: pi=3.14159265
  pmag=(magp**2/(8d0*pi))*( (R+h)/R)**(-6)
  RETURN
```

```
END FUNCTION pmag

!This function computes gas pressure
REAL(kind=8) FUNCTION pgas(h,Hx,M,R,mdot,sd,temp)
  IMPLICIT none
  REAL(kind=8) :: h,mdot
  REAL(kind=8), PARAMETER :: kb=1.38064881d-16
  REAL(kind=8) :: mue=1.17,mh=1.6726219d-24
  REAL(kind=8) :: M,R
  REAL(kind=8) :: density,temp
  REAL(kind=8) :: sd,Hx
  pgas=(kb/(mue*mh))*density(h,Hx,mdot,M,R,sd)*temp
  RETURN
END FUNCTION pgas

!radiation pressure as function of x,h obtained by equation [16]
REAL(kind=8) FUNCTION prad(Hx,h,M,R,mdot,sd)
  IMPLICIT none
  REAL(kind=8) :: lambda,M,R,Hx,h,rhoff,t,mdot,sd
  REAL(kind=8), PARAMETER :: mue=1.17,mh=1.6726219d-24
  REAL(kind=8), PARAMETER :: G=6.67259d-8
  REAL(kind=8), PARAMETER :: kt=0.3399371
  prad=(G*M/(R**2))*( 7.0d0*rhoff(M,R,mdot,sd,Hx)*Hx*&
      (lambda(Hx/R)-lambda(h/R)) + 2.0d0/( 3.0d0*kt*(1.0d0+Hx/R)**2.0d0)  )
  RETURN
END FUNCTION prad

!This function computes the first-guess temperature profile
REAL(kind=8) FUNCTION z_temperature(t,h,Hx,mdot,M,R,d0,sd)
  IMPLICIT none
  REAL(kind=8) :: t,h,Hmax,Hx
  REAL(kind=8) :: M,R,mdot
  REAL(kind=8), PARAMETER :: a=7.5646d-15
  REAL(kind=8), PARAMETER :: G=6.67259d-8
  REAL(kind=8) :: d0,sd
  REAL(kind=8) :: density
  z_temperature=( (3.0d0/a)*density(h*Hx,Hx,mdot,M,R,sd)*G*( M/(R+Hx))&
  *( (1.0d0-h) / (R/Hx+h) )*( 1.0d0-( 2.0d0*t/d0 )**2.0d0 ) )**0.25d0
  RETURN
END FUNCTION z_temperature

!This function computes the free-fall velocity
REAL(kind=8) FUNCTION vff(M,R,Hx)
  IMPLICIT none
  REAL(kind=8) :: M,Hx,R
  REAL(kind=8), PARAMETER :: G=6.67259d-8
  vff=sqrt(2d0*G*M/(R+Hx))
  RETURN
END FUNCTION vff

!This function computed the free-fall density via equation of continuity
REAL(kind=8) FUNCTION rhoff(M,R,mdot,sd,Hx)
  IMPLICIT none
  REAL(kind=8) :: mdot,sd,vff,Hx,M,R
  rhoff=mdot/(2.0d0*sd*vff(M,R,Hx))
  RETURN
END FUNCTION rhoff

!This function computes the density profile within the accretion column
REAL(kind=8) FUNCTION density(h,Hx,mdot,M,R,sd)!
  IMPLICIT none
  REAL(kind=8) :: M,R,h,Hx,mdot,sd,rhoff
```

```
  density=rhoff(M,R,mdot,sd,Hx)*( h/ (7.0d0*Hx) )**(-1)
  RETURN
END FUNCTION density

!This function computes the velocity profile within the accretion column
REAL(kind=8) FUNCTION velocity(h,Hx,M,R)
  IMPLICIT none
  REAL(kind=8) :: h,Hmax,M,R,Hx,vff
  velocity=vff(M,R,Hx)*( h/ (7.0d0*Hx) )
  RETURN
END FUNCTION velocity

!This function computes a first-guess on the geometrical shape of
!a vertical section of the accretion column, i. e. H(x)
REAL(kind=8) FUNCTION height(t,Hmax,R,d0)
  IMPLICIT none
  REAL(kind=8) :: t,Hmax,R,d0
  height=Hmax*(1-(2*t/d0)**2)
  RETURN
END FUNCTION height

!This function compute the Rosseland mean opacity
REAL(kind=8) FUNCTION xop(B,temp)
  IMPLICIT none
  REAL(kind=8) :: B,ecyc,temp
  REAL(kind=8), PARAMETER :: st=6.652458716d-25
  REAL(kind=8), PARAMETER :: mue=1.17,mh=1.6726219d-24
  REAL(kind=8), PARAMETER :: pi=3.1415926
  ecyc = 11.6d0*(B/1.0d12)
  xop = 20.0d0*(st/(mue*mh))*(2.0d0*pi**2/5.0d0)*( (temp/1.16d7)/ecyc )**2
  RETURN
END FUNCTION xop

!This function computes the multipolar magnetic-field strenght
REAL(kind=8) FUNCTION quadrupole(B,h,R)
  IMPLICIT none
  REAL(kind=8) :: B,h,R
  quadrupole=B*( (h+R)/R )**(-4.0d0)
  RETURN
END FUNCTION quadrupole

!This function results from the integration of the radiation
!pressure over the height from eq. [16]
REAL(kind=8) FUNCTION lambda(t)
  IMPLICIT none
  REAL(kind=8) :: t
  lambda=(1+t)**(-1)+log(t)-log(1+t)
  RETURN
END FUNCTION lambda

!This function is used in the machq program for re-calculating the
!new H(x) profile
REAL(kind=8) FUNCTION gfunc(x,sd,hb,M,R,mdot,P)
  IMPLICIT none
  REAL(kind=8) :: x !variable
  REAL(kind=8) :: P,kt,lambda,ff_rho,sd,hb,M,R,mdot
  REAL(kind=8), PARAMETER :: st=6.652458716d-25,G=6.67259d-8
  REAL(kind=8), PARAMETER :: mue=1.17,mh=1.6726219d-24
  kt=st/(mue*mh)
  ff_rho=(mdot/(2d0*sd))*sqrt( (R+x) / (2d0*G*M) )
  gfunc=(G*M/(R**2))*( 7d0*ff_rho*x*( lambda(x/R)-lambda(hb/R) ) + &
  2d0/(3d0*kt*((1d0+x/R)**2d0)) ) - P
```

```
  RETURN
END FUNCTION gfunc

!This subroutine gives an approximation of the solution
!of a nonlinear equation
REAL(kind=8) FUNCTION zero(xmin,xmax,num,vec)
  IMPLICIT none
  INTEGER :: j,num
  REAL(kind=8), DIMENSION(num) :: x,vec
  REAL(kind=8) :: dx,xmax,xmin,xA,xB,fA,fB,m
  dx=(xmax-xmin)/(num-1)
  DO j=1,num
    x(j)=xmin+(j-1)*dx
  END DO
  IF (vec(1)<0) THEN
     DO j=1,num
        IF (vec(j)<0) THEN
           CYCLE
        ELSE IF (vec(j)>0) THEN
           fA=vec(j-1)
           fB=vec(j)
           xA=x(j-1)
           xB=x(j)
           EXIT
        END IF
     END DO
  ELSE IF (vec(1)>0) THEN
      DO j=1,num
        IF (vec(j)>0) THEN
           CYCLE
        ELSE IF (vec(j)<0) THEN
           fB=vec(j-1)
           fA=vec(j)
           xB=x(j)
           xA=x(j-1)
           EXIT
        END IF
     END DO
  ELSE
     WRITE(*,*) 'Maybe NaN?',vec(1)
  END IF
  m=(fB-fA)/(xA-xB)
  zero=xA-fA/m
  RETURN
END FUNCTION zero

!This function computes the integral through the Trapezoidal Rule
REAL(kind=8) FUNCTION integrate(N,func,xin,xfin)
  IMPLICIT none
  INTEGER :: k,N
  REAL(kind=8), DIMENSION(N) :: func,psum
  REAL(kind=8) :: h,xin,xfin,par
  h=(xfin-xin)/(N-1)
  par=0
  DO k=1,N
     IF (func(k)==func(k)) THEN
        CYCLE
     ELSE IF (func(k)/=func(k)) THEN
        func(k)=func(k+1)
     END IF
  END DO
  DO k=2,N-1
```

```
     psum(k-1)=par+func(k)
     par=psum(k-1)
  END DO
  integrate=0.5*h*(func(1)+func(N)+2*par)
  RETURN
END FUNCTION integrate

!*****************************************************************************
!*                                      INVERSE                              *
!*                                    ---notes---                            *
!* a) f1 is the function to be inverted, represented with an array of       *
!*    dimension "dim";                                                       *
!* b) x is the independent variable of f1, represented with an array of     *
!*    dimension "dim":                                                       *
!* c) nx in the new independent variable, build with this subroutine and    *
!*    represented  with n array of dimension "ndim";                         *
!* d) ny is the inverse function of f1, build with this subroutine and      *
!*    available as output as a vector whose dimension is "ndim";             *
!* d) check is an integer parameter that allows to check whether            *
!*    the subroutine LINTERPOL has done correctly its work;                  *
!* IMPORTANT: RECALL that the new domain nx MUST be contained in the        *
!* codomain of f1!                                                          *
!* If in the main file the function to be inverted has a smaller codomain,  *
!* please compute a new vector that fulfills such requirement and then pass *
!* it as an argument for f1                                                 *
!*****************************************************************************
SUBROUTINE inverse(dim,ndim,nin,nfin,x,f1,nx,ny)
  IMPLICIT none
  INTEGER :: j
  INTEGER :: dim, ndim, check
  REAL(kind=8) :: nin,nfin,dnx,eps,linterpol
  REAL(kind=8), DIMENSION(dim) :: x,f1
  REAL(kind=8), DIMENSION(ndim) :: nx,ny,mny,mnx
  dnx=(nfin-nin)/(ndim-1)
  DO j=1,ndim
     nx(j)=nin+(j-1)*dnx
  END DO
  IF (f1(dim)-f1(1)>0) THEN
     DO j=1,ndim
        ny(j)=linterpol(dim,f1,x,nx(j),check)
     END DO
  ELSE IF (f1(dim)-f1(1)<0) THEN
     DO j=1,ndim
        mnx(j)=-nx(ndim-j+1)
        mny(j)=linterpol(dim,-f1,x,mnx(j),check)
     END DO
     DO j=1,ndim
        ny(j)=mny(ndim-j+1)
     END DO
  END IF
  RETURN
END SUBROUTINE inverse
!*****************************************************************************
!*                                                                           *
!*                                  L I N T E R P O L                        *
!*                                                                           *
!*  Subroutine:   LINTERPOL                                                  *
!*                                                                           *
!*  Programmer:   David G. Simpson                                           *
!*                NASA Goddard Space Flight Center                           *
!*                Greenbelt, Maryland  20771                                 *
!*                                                                           *
```

```
!*  Date:         October 29, 2013                                          *
!*                                                                          *
!*  Language:     Fortran-90                                                *
!*                                                                          *
!*  Version:      1.00a                                                     *
!*                                                                          *
!*  Description:  Piecewise liner interpolation.                            *
!*                                                                          *
!*  Notes:        Piecewise linear interpolation.  Given input arrays XX    *
!*                (independent variable) and YY (dependent variable),       *
!*                both of dimension NN, this routine finds, by linear       *
!*                interpolation, the value of Y(X).  Array XX must be in    *
!*                ascending order.                                          *
!*                                                                          *
!*                The flag IERR is returned as -1 if X is below the low     *
!*                end of XX (an error), +1 if X is above the high end       *
!*                of XX (also an error), or 0 if there was no error.        *
!****************************************************************************

      FUNCTION LINTERPOL (NN, XX, YY, X, IERR) RESULT (Y)

      IMPLICIT NONE

      INTEGER, INTENT(IN) :: NN
      DOUBLE PRECISION, DIMENSION(NN), INTENT(IN) :: XX, YY
      DOUBLE PRECISION, INTENT(IN) :: X
      INTEGER, INTENT(OUT) :: IERR
      DOUBLE PRECISION :: Y
      INTEGER :: I


      IF (X .LT. XX(1)) THEN                ! if below low end of XX (error)
         Y = YY(1)                          !  set Y = first YY value
         IERR = -1                          !  return error code -1
      ELSE IF (X .GT. XX(NN)) THEN          ! if above high end of XX (error)
         Y = YY(NN)                         !  set Y = last YY value
         IERR = +1                          !  return error code +1
      ELSE                                  ! if OK
         DO I = 2, NN                       ! loop to find first XX > X
            IF (XX(I) .GT. X) EXIT
         END DO
         Y = (YY(I)-YY(I-1))/(XX(I)-XX(I-1))*(X-XX(I-1))+YY(I-1)
         IERR = 0                           ! set error code to 0 (no error)
      END IF

      RETURN

      END FUNCTION LINTERPOL
```

Bibliography

M. A. Abramowicz, B. Czerny, and J. P. Lasota. *ApJ*, 1(332):646–658, 1988.

J. Arons. *ApJ*, 408(1):160–166, 1993.

M. Bachetti, F. A. Harrison, and D. J. Waltonothers. *Nature*, 514(1):202–204, 2014.

M. M. Basko and R. A. Sunyaev. *A&A*, 42(3):311–321, 1976.

K. Belczynski, T. Bulik, C. L. Fryer, et al. *ApJ*, 74(2):1217–1226, 2010.

V. Canuto, J. Lodenquai, and M. Ruderman. *Physical Review D*, 3(10):2303–2308, 1971.

E. J. M. Colbert and R. F. Mushotzky. *ApJ*, 519(1):89–107, 1999.

M. Dall'Osso, R. Perna, A. Papitto, et al. *MNRAS*, 449(2):2144–2150, 2015.

G. Fabbiano and G. Trinchieri. *ApJ*, 315:46–67, 1987.

S. Farrell, N. A. Webb, D. Barret, et al. *Nature*, 460(7251):73–75, 2009.

H. Feng and R. Soria. *New Astronomy Reviews*, 55(5):166–183, 2011.

J. Frank, A. King, and D. Rain. *Accretion Power in Astrophysics*, volume 1. Cambridge, 2002.

F. Fürst, D. J. Walton, F. A. Harrison, et al. *ApJ*, 831(2):6, 2016.

P. Ghosh. *Rotation and Accretion Powered Pulsars*. World Scientific, 2002.

P. Ghosh and F. K. Lamb. *ApJ*, 234:296–316, 1979, III.

J. C. Gladstone, T. P. Roberts, and C. Done. *MNRAS*, 397(4):1836–1851, 2009.

F. A. Harrison, W. W. Craig, F. E. Christensen, et al. *ApJ*, 770(2):19, 2013.

H. Herold. *Physical Review D (Particles and Fields)*, 19(10):2868–2875, 1979.

G. L. Israel, A. Papitto, P. Esposito, et al. *Monthly Notices of the Royal Astronomical Society*, 466(1):L48–L52, 2017a.

G. L. Israel, A. Belfiore, and L. Stella. *Science*, 355(6327):817–819, 2017b.

F. Jansen, D. Lumb, B. Altieri, et al. *A&A*, 365:L1–L6, 2001.

A. Kubota, T. Mizuno, K. Makishima, et al. *ApJ*, 547:L119–L122, 2001.

M. Mapelli, M. Colpi, and L. Zampieri. *MNRAS: Letters*, 395(1):L71–L75, 2009.

M. Mapelli, E. Ripamonti, L. Zampieri, et al. *MNRAS*, 408(1):234–253, 2010.

H. Matsumoto, T. G. Tsuru, K. Koyama, et al. *ApJ*, 547:L25–L28, 2001.

C. Motch, M. W. Pakull, R. Soria, et al. *Nature*, 514(7521):198–201, 2014.

S. E. Motta. *Astronomische Nachrichten*, 337:398, 2016.

R. Mushotzky. *Progress of Theoretical Physics Supplement*, 155:27–44, 2004.

A. A. Mushtukov, D. I. Nagirner, and J. Poutanen. *Physical Review D*, 85, 2012.

A. A. Mushtukov, V. F. Suleimanov, S. S. Tsygankov, and J. Poutanen. *MNRAS*, 447:1847–1856, 2015a.

A. A. Mushtukov, V. F. Suleimanov, S. S. Tsygankov, and J. Poutanen. *MNRAS*, 454:2539–2548, 2015b.

B. Paczyński. *Acta Astronomica*, 42:145–153, 1992.

D. Page and A. Sarmiento. *ApJ*, 473:1067, 1996.

J. Poutanen, G. Lipunova, S. Fabrika, et al. *MNRAS*, 377(3):1187–1194, 2007.

A. H. Prestwich, M. Tsantaki, A. Zezas, et al. *ApJ*, 769(2):9, 2013.

R. A. Remillard and J. E. McClintock. *Annual Review of Astronomy & Astrophysics*, 44:49–92, 2006.

G. B. Rybicky and A. P. Lightman. *Radiative Processes in Astrophysics*. Wiley, 2004.

N. I. Shakura and R. A. Sunyaev. *A&A*, 24:337 – 355, 1973.

H. Tananbaum, H. Gursky, E. Kellogg, et al. *ApJ*, 177:L5, 1972.

R. Taverna and R. Turolla. *arXiv:1705.01130*, 2017.

A. Tiengo, P. Esposito, S. Mereghetti, et al. *Nature*, 500(7462):312–314, 2013.

Y. M. Wang and J. Frank. *A&A*, 93:255–268, 1981.

K. Watarai, T. Mizuno, and S. Mineshige. *ApJ*, 549(1):L77–L80, 2001.

M. C. Weisskopf. *Space Telescopes and Instrumentation 2012: Ultraviolet to Gamma Ray. Proceedings of the SPIE*, 8443:9, 2012.

L. Zampieri and T. P. Roberts. *MNRAS*, 400(2):677–686, 2009.

S. Zane and R. Turolla. *MNRAS*, 366(3):727–738, 2006.